Journal of Energy Chemistry 59 (2021) 134–159

Contents lists available at ScienceDirect

Journal of Energy Chemistry

journal homepage: www.elsevier.com/locate/jechem

http://www.journals.elsevier.com/journal-of-energy-chemistry/

Review

Recent advances and perspectives on vanadium- and manganese-based cathode materials for aqueous zinc ion batteries

Na Liu [a], Bin Li [a], Zhangxing He [a,*], Lei Dai [a], Haiyan Wang [b,*], Ling Wang [a]

[a] School of Chemical Engineering, North China University of Science and Technology, Tangshan 063009, Hebei, China
[b] Hunan Provincial Key Laboratory of Chemical Power Sources, Hunan Provincial Key Laboratory of Efficient and Clean Utilization of Manganese Resources, College of Chemistry and Chemical Engineering, Central South University, Changsha 410083, Hunan, China

ARTICLE INFO

Article history:
Received 17 September 2020
Revised 20 October 2020
Accepted 25 October 2020
Available online 6 November 2020

Keywords:
Zinc ion batteries
Cathode
Vanadium-based materials
Manganese-based materials
Recent advances

ABSTRACT

The growing demand for energy storage has inspired researchers' exploration of advanced batteries. Aqueous zinc ion batteries (ZIBs) are promising secondary chemical battery system that can be selected and pursued. Rechargeable ZIBs possess merits of high security, low cost, environmental friendliness, and competitive performance, and they are received a lot of attention. However, the development of suitable zinc ion intercalation-type cathode materials is still a big challenge, resulting in failing to meet the commercial needs of ZIBs. Both vanadium-based and manganese-based compounds are representative of the most advanced and most widely used rechargeable ZIBs electrodes. The valence state of vanadium is +2 ~ +5, which can realize multi-electron transfer in the redox reaction and has a high specific capacity. Most of the manganese-based compounds have tunnel structure or three-dimensional space frame, with enough space to accommodate zinc ions. In order to understand the energy storage mechanism and electrochemical performance of these two materials, a specialized review focusing on state-of-the-art developments is needed. This review offers access for researchers to keep abreast of the research progress of cathode materials for ZIBs. The latest advanced researches in vanadium-based and manganese-based cathode materials applied in aqueous ZIBs are highlighted. This article will provide useful guidance for future studies on cathode materials and aqueous ZIBs.

Contents

* Corresponding authors.
E-mail addresses: zxhe@ncst.edu.cn (Z. He), wanghy419@126.com (H. Wang).

https://doi.org/10.1016/j.jechem.2020.10.044

Na Liu received her Bachelor's degree (2014–2018) in College of Chemical Engineering from North China University of Science and Technology. She is currently pursuing her master degree in chemical engineering and technology, North China University of Science and Technology. Her current research interest focuses on aqueous zinc-ion batteries.

Bin Li received her Bachelor's degree in College of Chemistry and Chemical Engineering from Central South University. She is currently pursuing her doctor degree in metallurgical engineering, North China University of Science and Technology. Her research interest is aqueous zinc-ion batteries.

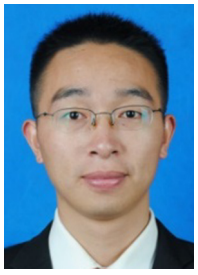

Zhangxing He is a professor at North China University of Science and Technology, China. He earned his Ph.D. from Central South University. His current research interests focus on the development of multifunctional nanomaterials for energy conversion and storage, including aqueous zinc-ion batteries, vanadium redox flow batteries, aqueous lithium-ion batteries.

Lei Dai received his Ph.D. degree from Yanshan University, China, in 2013. He is now a professor in North China University of Science and Technology. His current research focused on synthesis of nanomaterials and the potential applications in electrochemical devices.

Haiyan Wang earned his Ph.D. (2012) degree in Applied Chemistry at the Central South University. He once studied at the University of St. Andrews as a visiting Ph. D student. Starting in 2016, he worked for 2 years at the Hong Kong University of Science and Technology as a Hong Kong Scholar. Now he is an associate professor at College of Chemistry and Chemical Engineering at the Central South University. His current research interests focus on new energy materials and advanced batteries (Li/Na/Zn ion batteries and metal-air batteries). He has published over 100 refereed papers as the first or corresponding author.

Ling Wang received his Ph.D. degree from University of Science and Technology Beijing, China, in 1998. He is now a professor at North China University of Science and Technology, China. His current research interests focus on solid electrolytes, sensors, and high energy battery materials.

1. Introduction

Modern industrial civilization and economic society have a growing demand for electrical energy [1-3]. Developing electrochemical energy storage devices such as the rechargeable battery is the key to overcoming global energy challenges [4]. The most widely studied electrochemical rechargeable batteries are lithium-ion batteries [5-7]. The lithium-ion battery has dominated most of the energy storage market of portable electronic products for decades [8]. It is considered to be a possible battery system for smart grid and electric/hybrid vehicles. However, people's concerns about the low electrolyte safety, high cost, and limited lithium resources are increasing, which seriously restrict further development in large-scale application [9,10]. This situation promotes researchers to look for alternative opportunities in other rechargeable mental ion batteries, such as battery with monovalent (Na, K) or multivalent (Mg, Ca, Zn, Al) metal elements [11-14]. Potassium and sodium-ion batteries are plausible battery systems, given the similar chemical property of lithium, sodium, and potassium and relative abundance of sodium and potassium elements [15,16]. A lot of innovative progress has been achieved in the field of sodium-ion batteries and potassium ion batteries research in recent years. However, the low energy density, high operating cost, and safety issues remain a bottleneck [17].

Since the redox reaction involves multiple electrons, the system using polyvalent ions can obtain higher energy density and specific capacity in principle [18]. Aqueous aluminium ion batteries have been widely studied owing to the high volumetric capacity of

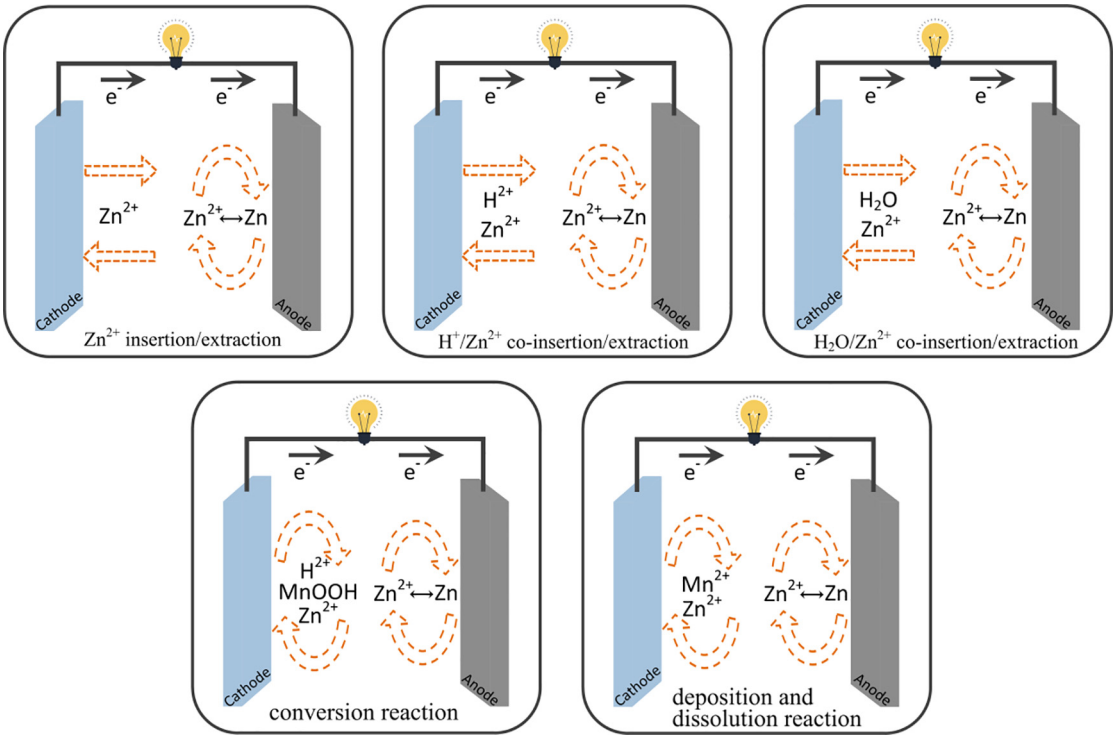

Fig. 1. General classification and schematic diagram of energy storage mechanisms of ZIBs.

about 8040 mAh cm^{-3} of aluminium anodes [19]. However, it is still greatly restricted by low power density and self-corrosion [20]. The passivation of Mg anode and the slow diffusion of Mg^{2+} in the matrix lattice have greatly hindered the migration of Mg^{2+} [21,22]. Therefore, finding available anode materials is vital to building a more powerful aqueous magnesium ion battery. ZIBs are novel secondary rechargeable aqueous batteries developed in last few years. This new type of battery has strong points of the simple preparation process, low cost, efficient and safe discharge process, high power density, and high energy density [23,24]. It presents promising application prospects in field of large-scale energy storage device.

ZIBs generally consist of a cathode which can accommodate zinc ions, an aqueous electrolyte, and a zinc metal anode [25]. The reaction mechanism of the aqueous ZIBs seems to be complicated, and it is still under intense discussion. In most ZIBs, zinc plating/stripping reactions occur at the metal zinc anode. And zinc ion intercalation/de-intercalation reactions occur in the cathode material [26,27]. Metallic zinc has been used in various batteries since Volta et al. applied zinc metal as an electrode in 1999, such as nickel-zinc batteries, zinc-manganese batteries, zinc ion batteries, and zinc-air batteries [28,29]. The theoretical capacity of zinc metal is as high as 820 mAh g^{-1}, and the oxidation–reduction potential is as low as −0.76 V vs. standard hydrogen electrode [30,31]. It owns characteristics of low cost, reliable safety and non-toxicity. Besides, zinc metal has another advantage, the zinc deposition and dissolution reactions of which occur more easily than Mg metal [32]. The electrolyte in ZIBs system is mildly neutral or weakly acidic. In neutral or weakly acidic solutions, zinc dendrites, and irreversible by-products such as $Zn(OH)_2$, ZnO are relatively few, compared with alkaline electrolytes [33,34]. Commonly used zinc salt solutions are $Zn(CF_3SO_3)_2$, $Zn(NO_3)_2$, $Zn(CH_3COO)_2$, $ZnSO_4$, and ZnCl, etc [35]. Also, the ionic conductivity of the aqueous electrolyte (≈1 S cm^{-1}) is much higher than that of non-aqueous electrolyte, about two orders of magnitude higher [37].

As early as the 1980s, people try to develop rechargeable ZIBs. Since 2015, exploration activities have surged globally in this field. Exploring some suitable cathode electrode material accommodating zinc ion intercalation/de-intercalation requires more effort. While developing, it is also facing some scientific and technological challenges. First, the higher charge of Zn^{2+} has the stronger electrostatic interaction with the cathode host. The electrostatic interaction between the crystal structure of the cathode material and divalent zinc ions is stronger than lithium ions [38]. To a certain extent, it is not conducive to the intercalation/ de-intercalation and ion diffusion for the cathode structure. For the storage and transportation of divalent carriers with greater mass, an open system with a broader spatial dimension needs to be built as a suitable cathode host. Second, the low conductivity of the cathode host, especially transition metal oxides, will slow down the reaction kinetics . It is not conducive to the electrode rate capability, resulting in direct capacity loss and poor electrochemical performance during charging and discharging. It is essential for practical applications. Third, part of the available highly oxidized transition metal ions dissolves in the two-electron transfer reaction, resulting in instability of the electrode and a decrease in capacity during long-term cycling. Finally, the accumulation of unnecessary reaction by-products on the electrode surface may hinder the smooth progress of the electrochemical reaction and cause a massive loss of cycle capacity.

So far, the cathode materials reported in the literature include vanadium-based compounds, manganese-based compounds, polyanionic compounds, Prussian blue analogues [40,41]. The valence state of vanadium element ranges from +2 to +5. Vanadium-based compounds are a vast family due to the diversity of vanadium oxide coordination, including vanadium oxide, vanadium phosphate, vanadate, and oxygen-free vanadium-based mixtures [42]. The crystal structure, chemical composition and electrochemical properties of vanadium-based materials are different. The vanadium-based mixture can realize multi-electron transfer in the redox reaction and has a higher capacity [43]. Due to its stable cycle performance and high specific capacity, many vanadium-based compounds have been developed as cathodes for ZIBs so far. Manganese-based compounds have the diversity

of crystal structure and oxidation state. Most of them have rich tunnel structure and three-dimensional space frame to support enough space to accommodate zinc ions [36]. It has been widely used as a high working voltage and considerable specific capacity ZIBs cathode material in recent decades. All in all, both vanadium-based and manganese-based compounds are forefront descriptions of the most advanced development for rechargeable ZIBs electrodes. Besides, the research of metal oxide cathode materials for ZIBs also helps to solve the problems of manganese cathode dissolution and low potential of vanadium oxide in the development of supercapacitors.

The electrochemical performance of the battery system largely depends on the type, structure and surface characteristics of the electrode material. The charge storage process of ZIBs relies on the migration of Zn^{2+} ions between two electrodes, so maintaining the stability of the cathode structure is very important. Vanadium-based and manganese-based compounds are the two most widely researched and applied materials in ZIBs, which have achieved excellent performance and been expected to reach more significant and more promising progress. This article mainly reviews the energy storage mechanisms and research progress of vanadium-based and manganese-based cathode materials in aqueous ZIBs, and designs to explore how to pave the way for the growth of aqueous ZIBs. It will attract more attention to discover new ZIBs electrode materials, clarify the electrode reaction mechanism, and promote their rapid development and practical application.

2. Energy storage mechanisms

ZIBs is a hot research field in recent years. Compared with insertion reaction mechanisms of other alkali metal ion battery, the reaction mechanism of ZIBs in aqueous solution is immature and problematic. The reaction mechanism involved in the energy storage process has always been a topic of debate. According to the existing research, many reaction mechanisms of ZIBs aqueous solutions have been proposed, including Zn^{2+} insertion/extraction, H^+/Zn^{2+} co-insertion/extraction, H_2O/Zn co-insertion/extraction, chemical conversion reaction mechanism, deposition and dissolution reaction mechanism, etc [44]. General classification and schematic diagram of energy storage mechanisms of ZIBs can be seen in Fig. 1.

2.1. Zn^{2+} insertion/extraction mechanism

By the reversible Zn^{2+} insertion/extraction, the early proposed energy storage mechanism of ZIBs is described in details. Kang and colleagues [27] first reported on the mild aqueous rechargeable ZIBs. They proposed to reversibly insert or extract Zn^{2+} into/from the α-MnO_2 cathode during discharge/charge. At the same time, the metal zinc anode would also undergo dissolution/deposition behaviour. This principle is entirely different from the two-step energy storage mechanism of alkaline zinc-manganese batteries. However, with the in-depth study of ZIBs, the energy storage mechanism of α-MnO_2 cathode is still controversial. There are also some clarifications on other various energy storage mechanisms of MnO_2, according to He and co-workers [45]. Subsequently, it was proved that the Zn^{2+} insertion/extraction mechanism will occur in β-, γ-, λ-, δ-MnO_2 [46,47].

Vanadium-based oxides are mainly layered/tunnelled/three-dimensional framework with large pore space, which is conducive to the insertion of Zn^{2+}. Nazar et al. [39] reported the intercalation reaction of zinc ions in the $Zn_{0.25}V_2O_5{\cdot}nH_2O$ electrode. They also described a fast and reversible intercalation/de-intercalation storage process of zinc ions. Each formula unit hosts more than one Zn^{2+} (capacity up to 300 mAh g^{-1}). First-principles calculations show that about 0.5 mol of Zn^{2+} can be inserted into the VO_2(B) cathode matrix material during the discharge process [48]. There are two parts in intercalation process of Zn^{2+}. First, insert 0.125 mol Zn^{2+} to form $Zn_{0.125}V_2O_5$ when the average potential is 0.78 V. Then discharge to 0.55 V, 0.375 mol Zn^{2+} continue to be inserted into the positive electrode to form $Zn_{0.5}V_2O_5$. Similar mechanisms exist in other vanadium-based compounds, such as $Li_xV_2O_5{\cdot}nH_2O$, $Ca_{0.25}V_2O_5{\cdot}nH_2O$, $Na_2V_6O_{16}{\cdot}3H_2O$, $Zn_3V_2O_7(OH)_2{\cdot}2H_2O$) [49]. Vanadium-based compounds evolve from V^{5+} to V^{4+} or even V^{3+} through the evolution of the V oxidation state, adapt to the intercalation of Zn^{2+}, and maintain a stable crystal framework.

2.2. H^+/Zn^{2+} co-insertion/extraction mechanism

The strong electrostatic repulsion of high charge valence and the large hydronium ion cause slow intercalation of Zn^{2+}. The intercalation of ions with high diffusion kinetics such as H^+ and Na^+ can promote the effective utilization of the active sites of the host structure and improve the ZIBs performances [50-52]. Wang et al. [53] first proposed the co-intercalation mechanism of hydrogen ions and zinc ions in Zn/ε-MnO_2 batteries, which is a typical example. The GITT and CV curves prove that the insertion of hydrogen ions occurs before the insertion of zinc ions, accompanied by the formation of MnOOH and then conversion to $ZnMnO_4$. A reversible H^+/Zn^{2+} co-insertion mechanism was also confirmed in α-MnO_2 cathode by Ji et al. [54]. First, insert H^+ into α-MnO_2 to enrich OH^- and form $[Zn(OH)_2]_3ZnSO_4{\cdot}5H_2O$. Then Zn^{2+} is inserted into the cathode host to form $ZnMn_2O_4$. It is found that the reversibility of Zn^{2+} insertion is not as good as that of H^+ insertion. Kang et al. [45] also found that during discharge, H^+ and Zn^{2+} were inserted into MOF-derived α-Mn_2O_3 sequentially. The morphology of the discharge product changes from flower-like to large flake-like.

The co-insertion mechanism is also found in the vanadium-based cathode. There is one simultaneous H^+/Zn^{2+} co-intercalation reaction when employing 1 M Na_2SO_4 + 1 M $ZnSO_4$ mixed electrolyte for $NaV_3O_8{\cdot}1.5H_2O$ cathode [55]. It can be expressed by the following formula:

$$NaZn_{0.1}V_3O_8 \cdot 1.5H_2O + 3.9H^+ + 0.4Zn^{2+} + 4.7e^- \rightarrow H_{3.9}NaZn_{0.5}V_3O_8 \cdot 1.5H_2O$$

Lighter protons improve the kinetics of zinc ion insertion and diffusion kinetics. It is worth noting that hydrogen and zinc ion shall be added at the same time rather than stepwise. However, the influence mechanism of H^+ on ions transfer needs further study.

2.3. H_2O/Zn^{2+} co-insertion/extraction mechanism

Structural water or interlayer cations can usually expand the layered structure of the material, which is conducive to hydrated Zn^{2+} intercalation. This mechanism is more common in vanadium-based compounds. For example, in V_2O_5, V_6O_{13} and $H_2V_3O_8$ electrodes [56,57], similar co-intercalation chemistry of water molecules and zinc ions can often be observed. The solvated water acts as a charge barrier, neutralizing the high charge density of Zn^{2+}, reducing the electrostatic interaction with the framework and promoting the transfer of Zn^{2+}. Mai et al. [58] proved that structured water plays a key role in the process of Zn^{2+} insertion. The effective charge of H_2O solvated Zn^{2+} is greatly reduced, thereby reducing the electrostatic interaction with the V_2O_5 framework and effectively promoting Zn^{2+} diffusion. Water molecules, Zn^{2+}, and $CF_3SO_3^-$ are inserted at the same time to maintain charge balance, and the distance between V_2O_5 layers is reduced from 12.6 Å to 10.4 Å when charged to 1.3 V. This can be attributed to the hydrogen bonds formed between Zn^{2+}, $CF_3SO_3^-$, H_2O and lattice

oxygen, which pull the V_2O_5 bilayer closer together. When discharge to 0.2 V, the bilayer distance increases from 10.4 Å to 13.5 Å. Cheng et al. [41] also found that, during the first discharge process, zinc ions and water molecules were inserted in V_2O_5 at the same time to generate an open-structured $Zn_{3+x}(OH)_2V_2O_7{\cdot}2H_2O$ host, and then reversible zinc ions deintercalation occurred. Similar to V_2O_5, water molecules can be inserted into V_6O_{13} electrode to form $Zn_aV_6O_{13}{\cdot}mH_2O$ and $Zn_xV_2O_7(OH)_2{\cdot}2H_2O$, and the next cycles depend on the intercalation/deintercalation of the zinc ions [59]. And huang et al. [60] found in the $Zn//NaCa_{0.6}V_6O_{16}{\cdot}3H_2O$ battery system, the structured water interlayer not only increases the channel spacing, providing a more convenient place for Zn^{2+} storage, but also accelerates the reaction kinetics. The electrochemical reactions for cathode are proposed as the following:

$$NaCa_{0.6}V_6O_{16}\cdot 3H_2O + 4.3Zn^{2+} + 8.6e^- \leftrightarrow Zn_{4.3}NaCa_{0.6}V_6O_{13}\cdot 3H_2O$$

Moreover, Tao et al. [61] found that the pre-insertion of Ca ion and water can significantly improve the reversible insertion/extraction stability of Zn^{2+} in manganese-based layered materials. Ca^{2+} and H_2O act as pillar for layered δ-MnO_2. Yu et al. [62] reported sodium ion and crystal water co-intercalated $Na_{0.55}Mn_2O_4{\cdot}0.57H_2O$ cathode. Sodium ions and crystal water can expand the distance between layers and accelerate the transport of zinc ions.

2.4. Conversion reaction mechanism

Compared with ion insertion chemistry, the conversion reaction in a battery can often provide a higher ability because the direct charge transfer in the reaction provides a superior theoretical specific capacity. Therefore, introducing a reasonable conversion reaction is a promising and effective method to construct high-performance ZIBs.

Liu et al. [63] demonstrated one Zn/α-MnO_2 system, with an operating principle of chemical conversion reaction mechanism. The protons in the water react with MnO_2. Then the MnOOH phase can be observed in the fully discharged state. The remaining OH^- will reacts with H_2O and $ZnSO_4$ in the solution to maintain the neutrality of the solution. The mechanism is as follows:

$$H_2O \leftrightarrow H^+ + OH^-$$

$$MnO_2 + H^+ + e^- \leftrightarrow MnOOH$$

$$\frac{1}{2}Zn^{2+} + OH^- + \frac{1}{6}ZnSO_4 + \frac{x}{6}H_2O \leftrightarrow \frac{1}{6}ZnSO_4\left[Zn(OH)_2\right]_3\cdot xH_2O$$

Qiao et al. [64] proposed multi-redox reactions during the galvanostatic charge and discharge process. The reversibility of water molecules participating in the redox reaction in the first cycle is poor. In the next cycle, hydrogen ions and zinc ions reversibly participate in the redox reaction, showed as following equation:

$$Mn^{2+} + H_2O \rightarrow MnO_2 + 4H^+ + 2e^-$$

$$MnO_2 + 4H^+ + 2e^- \leftrightarrow Mn^{2+} + 2H_2O$$

$$MnO_2 + H^+ + e^- \leftrightarrow MnOOH$$

$$MnO_2 + 0.5Zn^{2+} + e^- \leftrightarrow Zn_{0.5}MnO_2$$

In addition to this, there is a similar energy storage mechanism found in the β-MnO_2 and δ-MnO_2 electrode. Liu et al. [65] discovered H^+ conversion and Zn^{2+} intercalation in bulk δ-MnO_2. Kang et al. [66] proposed that there is a proton conversion mechanism in the β-MnO_2 cathode. In the first discharge cycle, β-MnO_2 is converted into MnOOH and dissolved into Mn^{2+}. In the next cycle, the deposited MnO_2 reacts with protons to form MnOOH and Mn^{2+}. Mn^{2+} is deposited as MnO_2 during the charging process. So, this is a combined mechanism of manganese deposition/dissolution and proton conversion reaction, showed as follows:

$$MnO_2 + H^+ + e^- \leftrightarrow MnOOH$$

$$MnOOH + 3H^+ + e^- \leftrightarrow Mn^{2+} + H_2O$$

$$4Zn^{2+} + SO_4^{2-} + 8H_2O \leftrightarrow Zn_4SO_4(OH)_6\cdot 5H_2O + 6H^+$$

2.5. Deposition and dissolution reaction mechanism

Somewhat different from the intercalation reaction or the conversion reaction is that there is a reversible MnO_x deposition reaction in manganese oxide. The pre-added Mn^{2+} additive ions are beneficial to the storage of active zinc on the electrode surface. Zn^{2+} insertion in the surface undissolved MnO_x layer, this phenomenon was found in spinel-type $ZnMn_2O_4$ by Kim et al. [67] as follows:

$$Mn^{2+}_{(electrolyte)} + xH_2O \leftrightarrow MnO_{x(surface)} + 2xH^+ + 2e^-$$

$$MnO_{x(surface)} + Zn^{2+}_{(electrolyte)} + 2e^- \leftrightarrow ZnMnO_{x(surface)}$$

Liang et al. [68] also discussed dissolution-deposition reaction mechanism in α- and δ-MnO_2 cathode with $MnSO_4$ and $ZnSO_4$ electrolyte. This reaction mechanism, rather than the ion insertion mechanism mainly contributes to the capacity of the battery. Tetravalent manganese is dissolved into divalent manganese ions. Then the birnessite-MnO_2 is reversibly deposited on the electrode surface during the discharge process. Lee et al. [69] that zinc ions are actually precipitated on the surface of α-MnO_2 in the form of layered zinc hydroxide sulfate ($Zn_4(OH)_6SO_4{\cdot}5H_2O$). During the discharge process, the cathode will produce trivalent manganese ions, and the trivalent manganese ions are unstable and prone to disproportionation, causing manganese to dissolve in the electrolyte. The pH of the electrolyte will rise until the precipitation reaction occurs. During the charging process, the pH decreases, and zinc hydroxide sulfate dissolves into the electrolyte. The reaction mechanism is as follows:

$$MnO_2 + 2H_2O + 2e^- \rightarrow Mn^{2+} + 2OH^-$$

$$3MnO_2 + 8Zn^{2+} + 2SO_4^{2-} + 16H_2O + 6e^- \rightarrow 3Mn^{2+} + 2Zn_4(OH)_6SO_4\cdot 5H_2O$$

In a little summary, the currently proposed ZIBs energy storage mechanism is complex and immature. The Zn^{2+} insertion/extraction, H^+/Zn^{2+} co-insertion/extraction, H_2O/Zn co-insertion/extraction are more common in vanadium-based compounds, and Zn^{2+} insertion/extraction, H^+/Zn^{2+} co-insertion/extraction, chemical conversion reaction mechanism, deposition and dissolution reaction mechanism mechanisms are more common in manganese-based compounds. The energy storage mechanism needs further clarification and exploration, which will help build a more efficient zinc ion battery system.

3. Vanadium-based cathode materials

The cathode material provides a zinc storage site, and to a large extent, determines the voltage and capacity of the ZIBs. Finding new cathode materials with better cyclability and larger capacity has become a subject of extensive research. Vanadium has the

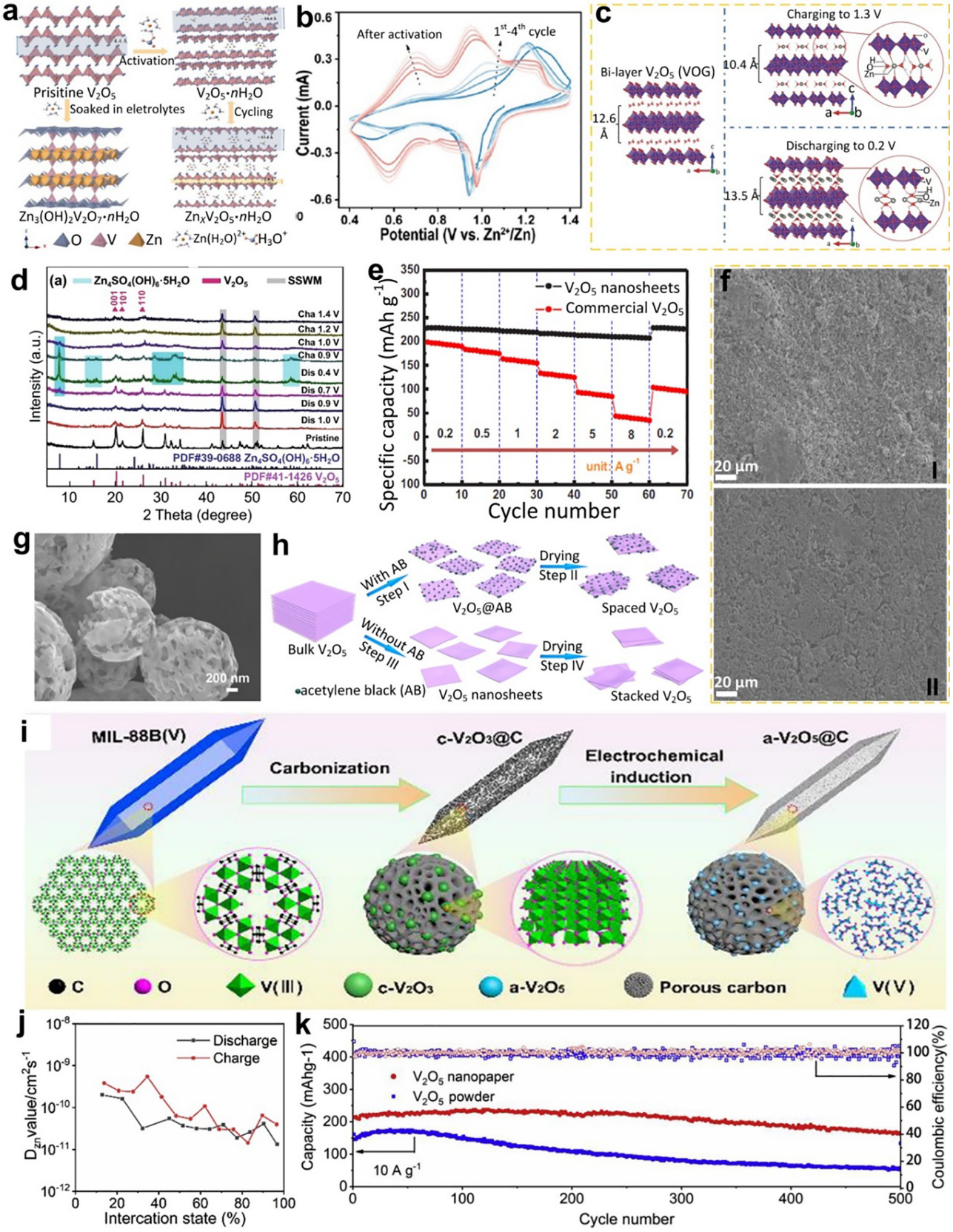
a
Activation
Prisitine V_2O_5
Soaked in eletrolytes
$V_2O_5 \cdot nH_2O$
Cycling
$Zn_3(OH)_2V_2O_7 \cdot nH_2O$
$Zn_XV_2O_5 \cdot nH_2O$
O V Zn
$Zn(H_2O)^{2+}$ H_3O^+
b
After activation
1st-4th cycle
Current (mA)
Potential (V vs. Zn2+/Zn)
c
Bi-layer V_2O_5 (VOG)
12.6 Å
Charging to 1.3 V
10.4 Å
Discharging to 0.2 V
13.5 Å
d
(a) $Zn_4SO_4(OH)_6 \cdot 5H_2O$ V_2O_5 SSWM
001 101 110
Cha 1.4 V
Cha 1.2 V
Cha 1.0 V
Cha 0.9 V
Dis 0.4 V
Dis 0.7 V
Dis 0.9 V
Dis 1.0 V
Pristine
PDF#39-0688 $Zn_4SO_4(OH)_6 \cdot 5H_2O$
PDF#41-1426 V_2O_5
Intensity (a.u.)
2 Theta (degree)
e
V_2O_5 nanosheets
Commercial V_2O_5
Specific capacity (mAh g-1)
0.2 0.5 1 2 5 8 0.2
unit: A g-1
Cycle number
f
20 μm
I
20 μm
II
g
200 nm
h
With AB
Step I
Drying
Step II
V_2O_5@AB
Spaced V_2O_5
Bulk V_2O_5
Without AB
Step III
Drying
Step IV
acetylene black (AB)
V_2O_5 nanosheets
Stacked V_2O_5
i
MIL-88B(V)
Carbonization
c-V_2O_3@C
Electrochemical induction
a-V_2O_5@C
C O V(III) c-V_2O_3 a-V_2O_5 Porous carbon V(V)
j
Discharge
Charge
D_{Zn} value/cm2s-1
Intercation state (%)
k
V_2O_5 nanopaper
V_2O_5 powder
10 A g-1
Capacity (mAhg-1)
Coulombic efficiency(%)
Cycle number

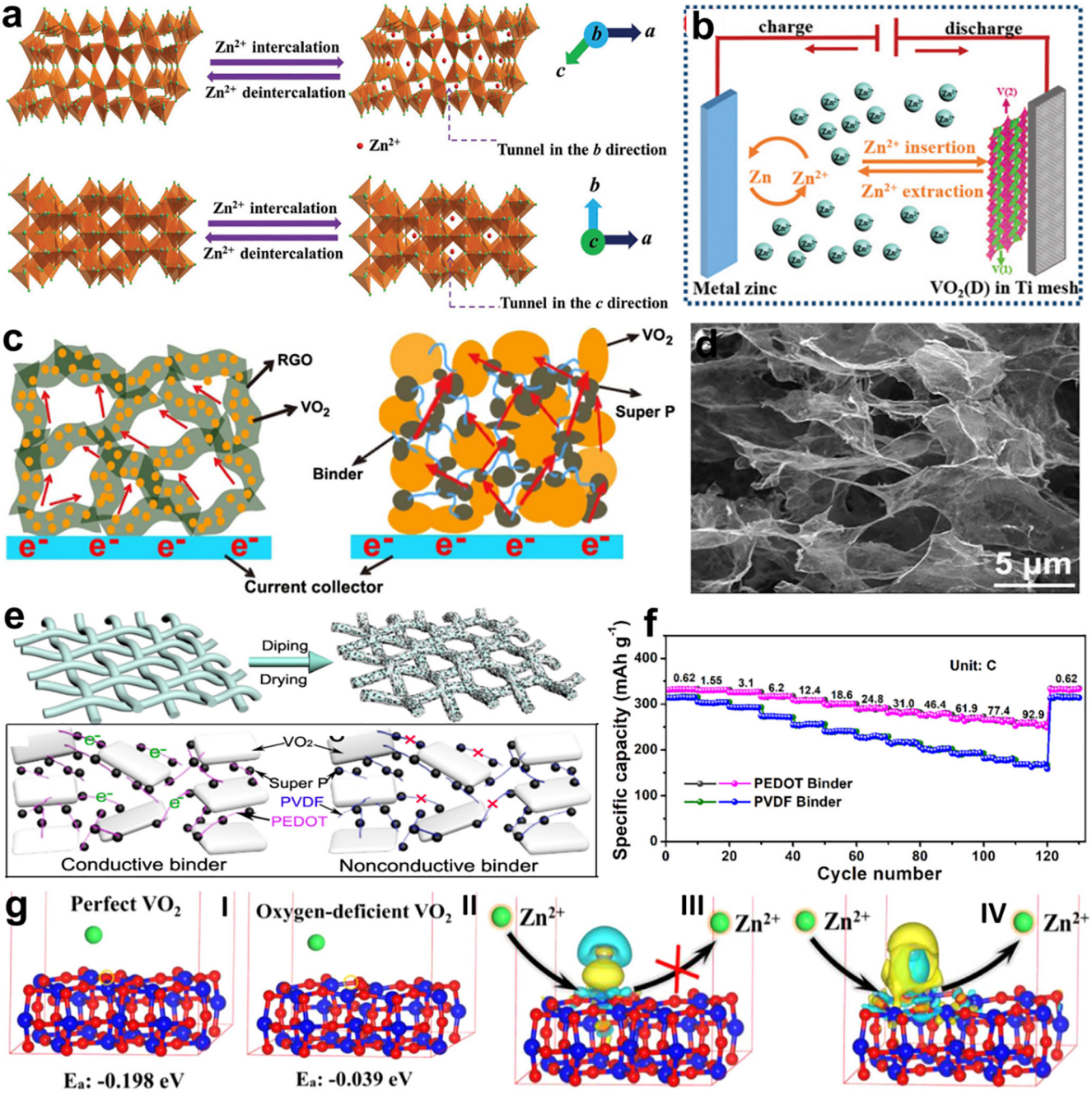

Fig. 3. (a) Schematic view of Zn^{2+} intercalation/de-intercalation VO_2(B) nanofibers projected along the direction of the b- and c-axes. Reproduced from Ref. [37] with permission from Wiley-VCH. (b) Schematic of the aqueous Zn/VO_2(D) secondary battery. Reproduced from Ref. [84] with permission from Royal Society of Chemistry. (c) Schematic illustration of electron transport in RGO/VO_2 freestanding film electrode and VO_2/super P electrode, (d) SEM image of RGO/VO_2 composite [85]. (e) Schematic illustrating the assembling strategy of VO_2 cathodes on the 3D current collector, schematic diagrams of the VO_2 cathodes with the conductive binder and nonconductive binder, (f) Rate performance at the current density ranging for 0.62C to 92.9C [86]. (g) The structural geometry (side view) of perfect VO_2 (I) and oxygen-deficient O_d-VO_2 (II) for Zn^{2+} adsorption. Color modes: red sphere for O, blue sphere for V, and green sphere for Zn. An oxygen vacancy was marked by orange cycle, Charge density and schematic illustrations for Zn^{2+} storage/release on perfect VO_2 (III) and oxygen-deficient O_d-VO_2 (IV). The yellow and blue color areas represent the charge accumulation and depletion regions, respectively [87].

Fig. 2. (a) Schematic illustration of the energy storage mechanism during activation and cycling process, (b) CV curves of yolk-shell V_2O_5//Zn battery at a scan rate of 0.1 mV s^{-1}. Reproduced from Ref. [77] with permission from Royal Society of Chemistry. (c) The proposed crystal structures of pristine VOG, VOG after charging to 1.3 V, and discharging to 0.2 V. Reproduced from Ref. [58] with permission from Wiley-VCH. (d) Ex situ XRD patterns of V^{4+}-V_2O_5 electrodes discharged or charged to different voltage states at the current density of 100 mA g^{-1}. Reproduced from Ref. [78] with permission from Springer Nature. (e) Rate specific capacity curves of V_2O_5 nanosheets and commercial V_2O_5 at various rates, (f) SEM images of V_2O_5 nanosheets electrode: pristine(I) and 200th cycle (II). Reproduced from Ref. [79] with permission from Electrochemical Society. (g) SEM image of porous V_2O_5 microspheres using sucrose as a carbon source. Reproduced from Ref. [80] with permission from Royal Society of Chemistry. (h) Schematic illustration of the strategy with and without in-situ adding AB spacer to prepare spaced V_2O_5 and stacked V_2O_5. Reproduced from Ref. [81] with permission from American Chemical Society. (i) Schematic illustration of the fabrication of V_2O_5@C electrodes. Reproduced from Ref. [82] with permission from Wiley-VCH. (j) Calculated diffusivity coefficient of Zn^{2+} of V_2O_5 nano paper in the first cycle, (k) Cycle performance of the V_2O_5 nano paper and the V_2O_5 powder electrode at 10 A g^{-1} [23].

characteristics of variable valence states, low cost and abundant resources [70]. The common valences of vanadium are +2, +3, +4, and +5, so it can undergo redox reactions with multi-electron transfer and exhibit high capacity properties. Common vanadium-based compounds mainly include vanadium-based oxides, vanadium-based phosphates, etc. Moreover, vanadium-based compounds usually have different crystal structures and electrochemical properties. They have varieties of open structures, which facilitate the insertion/extraction of ions. Vanadium-based materials are important electrode materials in battery systems, especially in sodium-ion battery and lithium-ion battery [71,72]. In recent years, vanadium-based compounds have also received extensive attention in aqueous ZIBs [73]. They have a higher capacity than manganese-based compounds, but the discharge voltage is slightly lower.

3.1. V_2O_5

V_2O_5 is a typical layered vanadium-based compound, in which V atoms and O atoms form a [VO_5] square pyramid and further form a layered structure by co-apex or co-edge [44]. Van der Waals force can connect adjacent layers, and the layer spacing is about 0.58 nm. In recent years, there are many investigation performed about V_2O_5, which has been a high-performance intercalation cathode with good cycle stability and high energy density for ZIBs. As we know, the structure of electrode material makes a significant influence on the electrochemical performance of batteries. Therefore, it is significant to study V_2O_5 with different structures. V_2O_5 samples with various morphologies, such as hollow spheres, sheets, rods, and flowers, can be synthesized by various methods [74,75].

Yang et al. [76] synthesized spherical V_2O_5 by a solvothermal method for rechargeable ZIBs. The porous hollow spheres and fragments can be seen in the morphology, while the structure of commercial V_2O_5 is irregular. The sample has a smaller particle size and larger specific surface area, which makes it in good contact with the electrolyte. And the larger layer spacing is conducive for the intercalation of high positive electricity of Zn. Compared with commercial V_2O_5, this hollow sphere exhibits much better rate capacity and cycle stability. When the current density is 10 A g^{-1}, the specific discharge capacity and capacity retention rate are as high as 132 mAh g^{-1} and 82.5% after 6200 cycles. Li et al. [77] proposed an anhydrous yolk-shell V_2O_5 via a facile template-free solvothermal method. Due to its porous yolk-shell structure, this V_2O_5 can promote electrolyte transport and inhibit structural collapse greatly during cycling. After the activation process of co-intercalation of hydrogen ions and zinc ions (Fig. 2a), the charge transfer resistance of electrode is reduced, and the electrochemical activity and reversibility of the electrode are significantly enhanced (Fig. 2b).

Because of the strong interaction between divalent zinc ion and matrix lattice, the intercalation/de-intercalation of zinc ions is slow. The low electronic conductivity of V_2O_5 and the slow intercalation/de-intercalation of zinc ions seriously hinder its practical application in ZIBs. Some groups have disclosed that structural water played a key role in the insertion process of Zn^{2+} into $V_2O_5{\cdot}nH_2O$ bilayers. Mai et al. developed the $V_2O_5{\cdot}H_2O$/graphene (VOG) cathode material [58]. This material shows excellent reversible intercalation/de-intercalation property of zinc ions. They confirmed that the structural water plays the function of charge shielding to metal ions. By reducing the effective charge, the electrostatic interaction between metal ions and V_2O_5 framework can be reduced. Then the zinc ion diffusion can be effectively promoted. Water molecules like lubricants accelerate the transport of zinc ions. The energy density and capacity of zinc ion batteries are high. The hydrogen bond formation between lattice oxygen $CF_3SO_3^-$, Zn^{2+}, and water bring the VOG bilayer closer together (Fig. 2c). Cheng et al. [41] synthesized porous V_2O_5 nanofibers, and reported a phase transition reaction mechanism. The water molecules and Zn^{2+} are inserted into V_2O_5 during the first discharge. And this cathode enables a high capacity retention of 81% at 20 mA g^{-1} after 500 cycles.

To increase the electronic conductivity, Liang et al. [78] firstly constructed hollow V^{4+}-V_2O_5 nanospheres using VOOH as the precursor. This cathode exhibits excellent cycling performance and rate capability. The presence of V^{4+} leads to higher conductivity, and faster ion diffusion, thus higher electrochemical activity. As seen in Fig. 2d, it is worth noting that during the discharge, there is the new phase of $Zn_4SO_4(OH)_6{\cdot}5H_2O$ formed. The diffraction peak positions of (001), (101) and (110) lattice planes are almost unchanged, demonstrating that V_2O_5 is still layered structure during charging and discharging process. Furthermore, Chen et al. [79] successfully rearranged the structure of commercial V_2O_5 and prepared V_2O_5 nanosheets doped by low-valence V ions using oxalic acid as reductant. V_2O_5 nanocrystals after structural rearrangement and V^{4+} doping possesses broader lattice parameters and smaller grain sizes, indicating higher electronic conductivity and

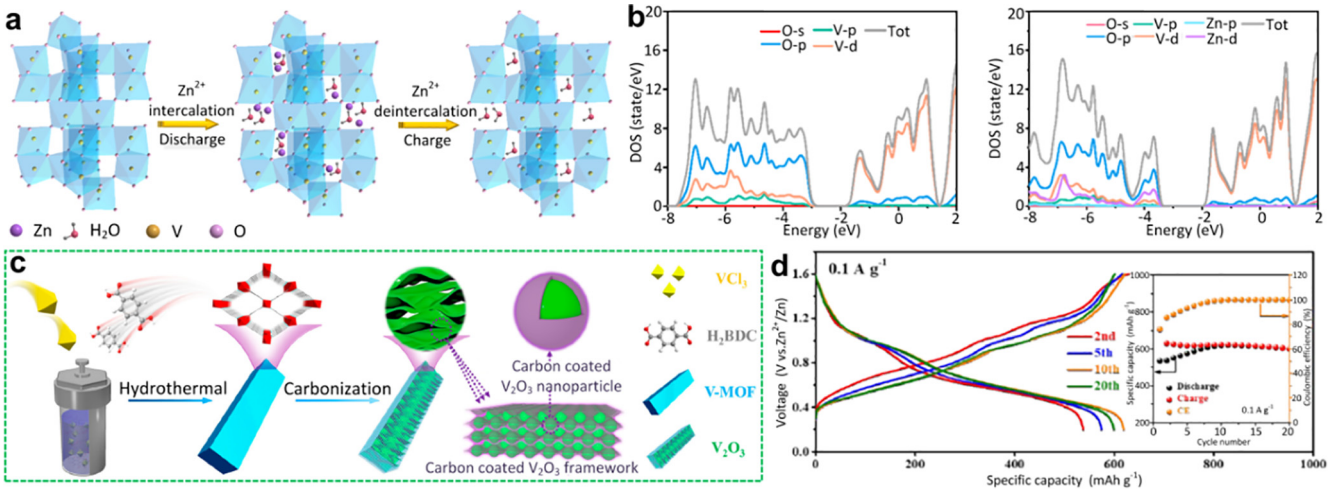

Fig. 4. (a) Schematic illustrations of Zn^{2+} storage mechanism of V_2O_3 cathode during the processes of discharge and charge, (b) The PDOS of V_2O_3 without (left) and with (right) Zn ions. Reproduced from Ref. [89] with permission from American Chemical Society. (c) Schematic illustration of the fabrication of the hierarchical carbon-coated V_2O_3, (d) GCD curves of V_2O_3 in 2 M $Zn(CF_3SO_3)_2$ aqueous electrolyte at 0.1 A g^{-1}. Reproduced from Ref. [90] with permission from American Chemical Society.

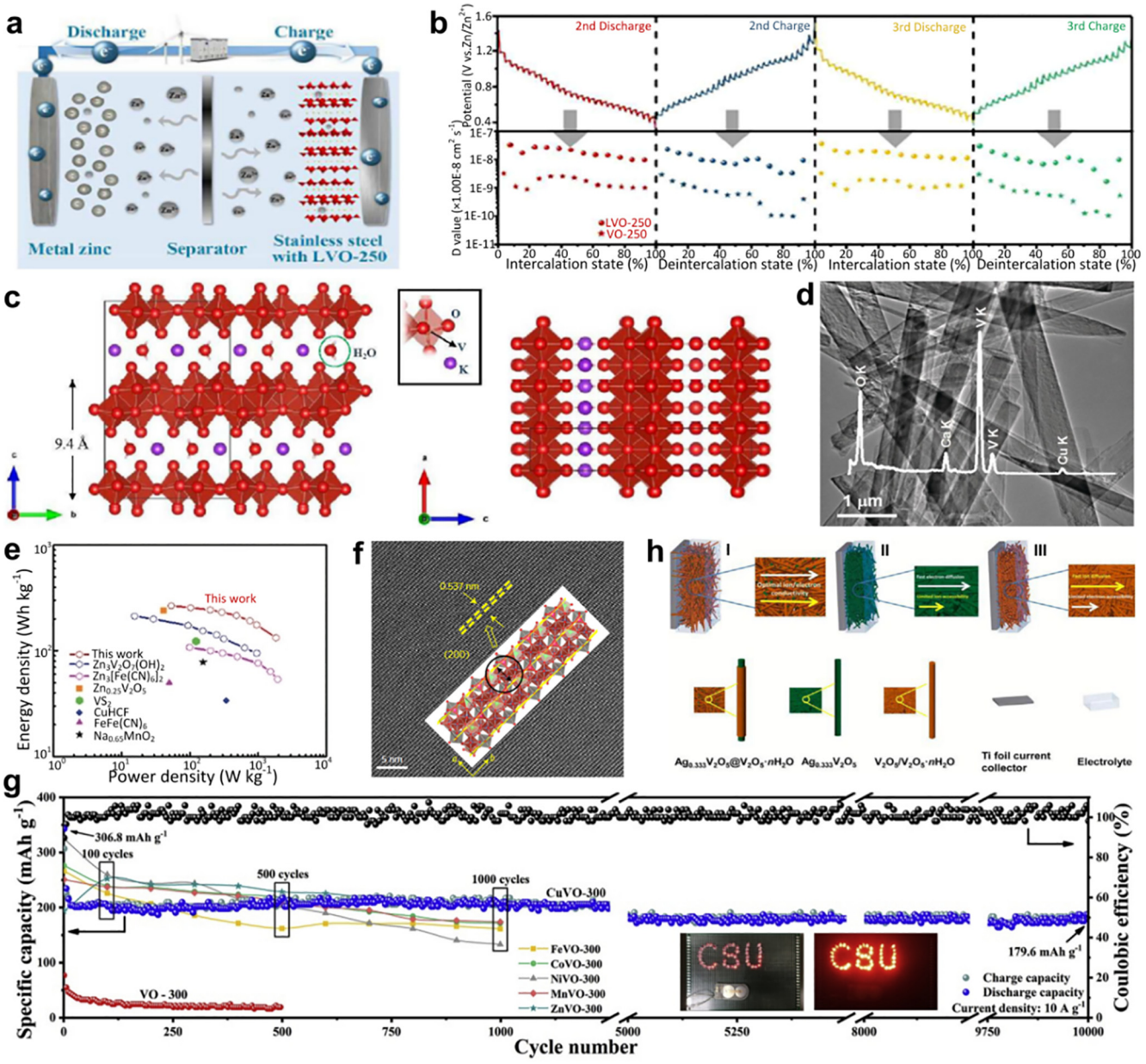

Fig. 5. (a) The working principle of Metallic zinc//LVO-250 aqueous ZIBs, (b) The discharge/charge curves in Ganlvanostatic Intermittent Titration Technique measurement of LVO-250 and corresponding diffusivity coefficient of Zn^{2+} in discharge and charge processes of LVO-250 and VO-250 samples in the 2nd and 3rd cycles. Reproduced from Ref. [96] with permission from Royal Society of Chemistry. (c) The illustration of KVO crystal structure viewed along different axes. Reproduced from Ref. [97] with permission from Royal Society of Chemistry. (d) TEM images of CVO nanobelts (inset: the EDS spectrum of as-obtained CVO). (e) The Ragone plot of Zn//CVO cell in comparison with other aqueous ZIBs. Reproduced from Ref. [98] with permission from Wiley-VCH. (f) Lattice-resolved HRTEM image and crystallographic model of the structure of $Zn_{0.25}V_2O_5{\cdot}nH_2O$ nanobelts. Reproduced from Ref. [39] with permission from Springer Nature. (g) Long-term cycling performances of samples at 10 A g^{-1} with a lamp panel illuminated by four Zn//CuVO-300 coin cells [11]. (h) Schematic illustration of the ion/electron percolating states in varied electrodes (I: the $Ag_{0.333}V_2O_5@V_2O_5{\cdot}nH_2O$ electrode, II: the pure $Ag_{0.333}V_2O_5$ electrode, III: the $V_2O_5/V_2O_5{\cdot}nH_2O$ electrode). Reproduced from Ref. [101] with permission from Royal Society of Chemistry.

better electrochemical performance (Fig. 2e). The surface of electrode is unchanged, and almost no cracks can be seen after 200 cycles (Fig. 2f), indicating the stable structure of V_2O_5 nanosheets.

Carbon coating or adding conductive agents is also an effective method to ameliorate the conductivity. Carbon coated porous V_2O_5 microspheres using sucrose, polyvinyl pyrrolidone and oxalic acid as carbon source were synthesized by spray drying method [80]. In this case, the porous structure (Fig. 2g) can effectively shorten the ion transport length. It can also buffer the volume change during the zinc ion intercalation/delamination process. Wang et al. [81] constructed a V_2O_5 nanosheet (Fig. 2h) with in-situ acetylene black spacer. In-situ acetylene black spaced V_2O_5 nanosheet electrodes provides fast charge transfer kinetics, improved conductivity and a wealth of active sites on the electrolyte/electrode interface. Niu et al. [82] used in-situ electrochemical induction for the first time to prepare MOF-derived amorphous V_2O_5 and carbon composite materials (Fig. 2i). The porous carbon framework provides continuous ion diffusion channels and electron transport channels. Amorphous V_2O_5 has more active sites and isotropic Zn^{2+} diffusion routes, which makes Zn^{2+} transport faster and has a larger specific capacity. In addition, V_2O_5 nanopaper consisting of multiwall carbon nanotubes and V_2O_5 nanofibers was constructed [23]. Carbon

nanotubes wrapped in V_2O_5 nanofibers are excellent electronic conductive networks. As a result, the dynamics process of Zn^{2+} is increased to 1.32×10^{-12}–3.82×10^{-11} cm^2 s^{-1} (Fig. 2j). When used as cathode material in ZIBs, it delivers an initial capacity of 341.3 mAh g^{-1} and maintains 335.1 mAh g^{-1} at 1 A g^{-1} over 100 cycles (Fig. 2k).

3.2. VO_2

There are several different crystal forms of vanadium dioxide (VO_2), including stable monoclinic VO_2(M), rutile-type VO_2(R), tetragonal VO_2(A) and VO_2(C), and metastable VO_2(B). VO_2 has a tunnel-type structure, and the lattice spacing is large enough for Zn^{2+} to be easily inserted/extracted [37]. There is greater resistance to lattice shear to resist the insertion/extraction of zinc ions [83]. Therefore, it will have better structural stability. Yang et al. [37] synthesized VO_2(B) nanofibers by hydrothermal method. They found ultrafast kinetics and intercalation pseudocapacitance behaviour VO_2(B) nanofibers. Because VO_2(B) nanofibers have unique tunnel transport channels along the b-axis and c-axis (Fig. 3a), the structure changes little when Zn^{2+} is intercalated, which eliminates the limitation of solid-state diffusion in the vanadium dioxide electrode. Yang et al. [84] prepared monoclinic VO_2(D) hollow nanospheres via a simple template-free hydrothermal method. Their research has revealed the Zn^{2+} insertion/extraction energy storage mechanism (Fig. 3b).

In addition to the electrode stability, the transport of Zn^{2+} and electrons also plays a significant role in the power supply capability of ZIBs. The transport of Zn^{2+} and electrons in traditional cathodes is affected by the addition of binders. For this reason, Liu et al. [85] developed rGO/VO_2 composite films without binders. The continuous three-dimensional porous structure not only provides an effective way for electrons and Zn^{2+} transfer (Fig. 3c), but also alleviates a large amount of deformation caused by Zn^{2+} insertion/extraction. Its excellent mechanical properties make it capable of being used as a flexible ZIBs electrode. In addition to satisfactory energy density, it also has better cycle performance and rate performance. Electrolyte ions can easily contact with the ultra-thin nano VO_2 (Fig. 3d) on the graphene to ensure the progress of the redox reaction. Sun et al. [86] used carbon fibre cloth and PEDOT as a 3D current collector and conductive binders, respectively (Fig. 3e). VO_2 is connected to Super P and PEDOT binders, allowing electrons to be transported quickly and continuously between the VO_2 electrode and the collector. Compared with nonconductive binders, batteries assembled with conductive binders provide higher capacity (Fig. 3f). Wang et al. [87] synthesized 3D spongy VO_2 composite with grapheme modified and rich oxygen vacancies. DFT calculations confirmed that oxygen vacancies can effectively adjust the adsorption energy of Zn^{2+}, leading to reversible adsorption/desorption of Zn^{2+} (Fig. 3g). At the same time, the heterogeneous interface modified by graphene makes the rapid transfer of electrons.

3.3. V_2O_3

V_2O_3 is a typical corundum structure with metallic behaviour, and electrons in the 3d orbital of vanadium can be transported along the V-V chain. Besides, its inherent three-dimensional open-hole structure facilitates the rapid diffusion of Zn^{2+}. It is widely used in lithium-ion batteries and sulfur-ion batteries [88]. Hu et al. [89] reported the porous and highly conductive V_2O_3@C nanospheres material, and indicated its application as an intercalation cathode for aqueous ZIBs. The proper pore distribution and unique channels of corundum V_2O_3 help the rapid insertion and extraction of zinc ions, and the carbon skeleton gives the structure cyclic stability. The research mechanism shows that it is necessary to insert water molecules and zinc ions into the material at the same time (Fig. 4a). After zinc ion doping, the energy gap between high and low energy part is larger, indicating electrons are more localized (Fig. 4b). The orbital hybridization of these atoms is strong, and the structure with Zn inserted can be more stable.

Dou et al. [90] have synthesized the V_2O_3 micro cuboids through a MOF-oriented two-step method (Fig. 4c), and demonstrated that through an in-situ anodic oxidation strategy, V_2O_3 could be a high-performance cathode material. By adjusting the morphology of the V_2O_3 sample and the electrolyte concentration at the same time, the first charge process can realize the V_2O_3 cathode super-efficient oxidation. Reversible capacity is 625 mAh g^{-1} and 605 mAh g^{-1} after 10 and 20 cycles (Fig. 4d), corresponding to 1.75 electron transfer. Zn//V_2O_3 batteries deliver satisfactory power (13 kW kg^{-1} at 20 A g^{-1}) density and energy (406 Wh kg^{-1} at 0.1 A g^{-1}) density.

3.4. $M_xV_2O_5$

V_2O_5 is an ideal host of multivalent metal ions in the battery system. However, diffusion kinetics of Zn^{2+} in V_2O_5 cathode in aqueous solution is low due to the narrow layer spacing. Fortunately, metal ions can play an auxiliary role in the cathode, which is beneficial to rapid ion diffusion and prevents collapse of the layer structure when intercalating and deintercalating guest ions [5,91,92]. Vanadates can improve the diffusion kinetics of ions during the charge and discharge process. Guest ions such as Zn^{2+} can enter and diffuse freely, resulting in a high rate and cycle ability. During the charge/discharge process, in order to improve the structural stability and realize the rapid and reversible intercalation/deintercalation reaction of Zn^{2+}, the pre-intercalated metal ions can be used as pillars. However, these pre-intercalated metal ions may cause the change of the initial structure of V_2O_5, and the insertion of a large number of metal ions may reduce the specific capacity of V_2O_5-based materials. Therefore, the type and quantity of pre-intercalated metal ions is a problem worthy of further study.

$M_xV_2O_5$ compounds (M = alkali, alkaline earth metals, other metals) have been widely studied [93–95]. The pre-intercalation of alkali metal in the layered vanadium oxide can be used as a pillar to expand the interlayer spacing and improve ion diffusion during charge and discharge. For example, $Li_xV_2O_5{\cdot}nH_2O$ was developed by one-step hydrothermal process as a cathode material [96]. Fig. 5a displays the working process of this battery. As shown, when Li ions exist, the distance between the V_2O_5 layers increases. Compared with V_2O_5, the diffusion kinetics of Zn^{2+} between the molecular layers is increased (Fig. 5b). The sample annealed at 250 °C displays a superior rate capability with an average specific capacity of 470, 316 and 190 mAh g^{-1} at current density of 0.5, 2 and 8 A g^{-1}, respectively. EIS test indicates that the resistance of battery decreases with test temperature increasing. Kim et al. [97] has successfully prepared K doped V_2O_5 (KVO) nanorods using simple hydrothermal technology. The excellent performance of the cathode is due to the low Zn^{2+} migration barrier, high conductivity and low surface energy brought by its unique exposed layer structure. The potassium ions between the layers (Fig. 5c) act as pillars to support the layer structure and shield the zinc ion from the high charge density. It not only enlarges the interlayer distance, but also maintains the structure and electrochemical stability during charging and discharging. Alshareef et al. [98] prepared $Ca_{0.24}V_2O_5{\cdot}0.83H_2O$ nanobelts with several microns in length and several hundred nanometers in width as a cathode. The typical TEM images (Fig. 5d) further illustrate the single crystallinity and flat ribbon morphology of this material. For comparison, alkaline earth metals can produce stronger ionic bonds than alkali metals, leading to a much better combination of the layers, thus effectively preventing collapsing of the host structure during the cycling. At a power density

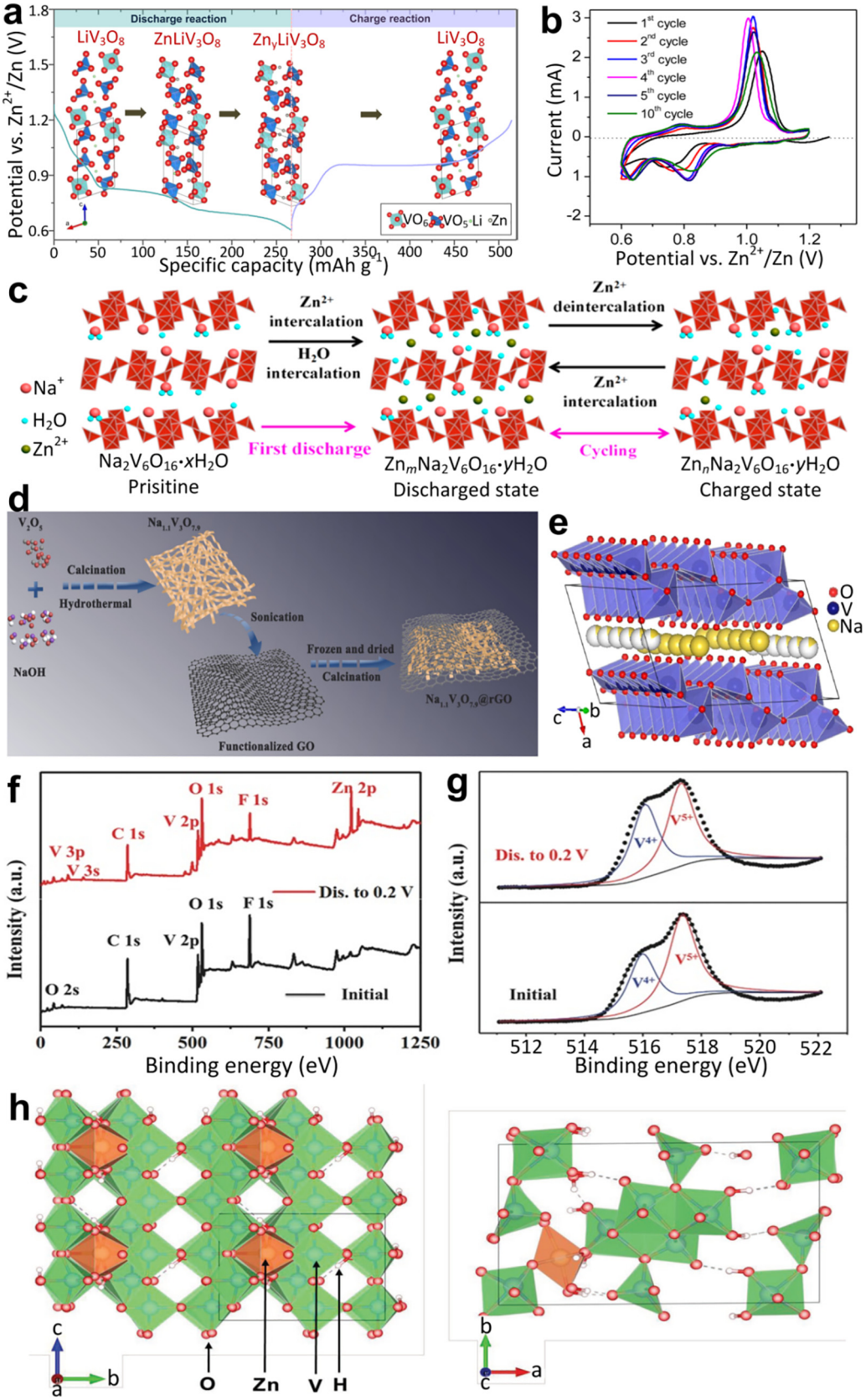

Fig. 6. (a) Schematic of the Zn-intercalation mechanism in the present LiV_3O_8 cathode, (b) Cyclic voltammetry measurements of LiV_3O_8 cathode performed at 0.5 mV s^{-1} scan rate. Reproduced from Ref. [103] with permission from American Chemical Society. (c) Schematic illustrations of water intercalation accompanying Zn^{2+} intercalation into $Na_2V_6O_{16}{\cdot}1.63H_2O$ nanowires electrode at the first discharge process and Zn^{2+} deintercalation and intercalation upon electrochemical charge and discharge processes. Here, $x < y$ and $m > n$. Reproduced from Ref. [104] with permission from American Chemical Society. (d) Illustration of synthesis procedure of pilotaxitic $Na_{1.1}V_3O_{7.9}$ nanoribbons/grapheme, (e) The structural framework of $Na_{1.1}V_3O_{7.9}$ [105]. (f) XPS spectra of $H_2V_3O_8$ electrodes, (g) Corresponding high resolution XPS spectra of vanadium at the initial state and the full discharge state. Reproduced from Ref. [110] with permission from Wiley-VCH. (h) Potential intercalated Zn sites in the $H_2V_3O_8$ crystal viewed along the [98] direction and along the [001] direction. Reproduced from Ref. [111] with permission from Wiley-VCH.

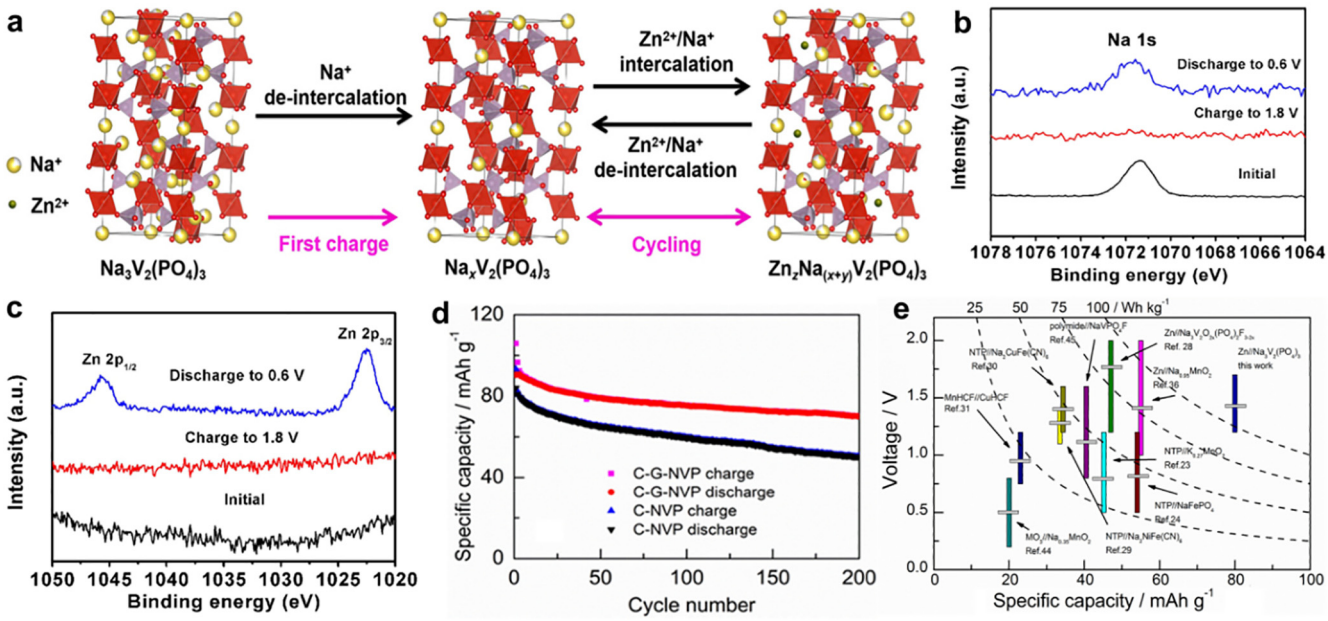

Fig. 7. (a) Schematic illustrations of ions deintercalation/intercalation from/into the NVP@rGO during charge/discharge processes, (b-c) XPS spectra of Na 1s and Zn 2p of the NVP@rGO microspheres in its original, charged, and discharged states [117]. (d) Cycling performance at charge/discharge rate of 0.5C of two samples. (e) Comparison of energy density of some typical aqueous rechargeable batteries [118].

of 53.4 W kg^{-1}, Zn//$Ca_{0.24}V_2O_5{\cdot}0.83H_2O$ cell can demonstrate a high energy density of 267 Wh kg^{-1}, exceeding most of the previously reported results (Fig. 5e).

The performance of intercalation rechargeable battery relies on the combination of main electrodes and guest ion species. Preintercalation of other metal ions (Fe, Co, Ni, Mn, Zn, Cu, Ag, etc.) in V_2O_5 interlayers can significantly improve its ion diffusion kinetics, conductivity, and structural stability during the cycling [99]. This strategy also has the advantages of high capacity, good long-term cycle stability, suitable wide temperature property, etc. Nazar and co-workers [39] synthesized the $Zn_{0.25}V_2O_5{\cdot}nH_2O$ single-crystal nanobelt by microwave hydrothermal technology. HRTEM image and crystallographic model of the structure (Fig. 5f) show 200 crystal planes, confirming the single-crystal nature which grows along the b direction. Crystal water and the interlayer metal ion in the layered oxide act as pillars to provide structural stability during repeated cycles. The spacious layered structure also allows water molecules to be inserted into the interlayer space from the electrolyte, further expanding the channel for easy intercalation of Zn^{2+}, enabling it to provide high discharge capacity. The inherent zinc ions stabilize this layered structure, thereby ensuring the stability of long-term circulation and helping to satisfy the basic requirements of large-scale storage application. Zhou et al. [11] chemically intercalated a small amount of transition metal ions (Cu^{2+}, Zn^{2+}, Mn^{2+}, Ni^{2+}, Co^{2+}, Fe^{2+}) into V_2O_5 intermediate layer by hydrothermal method. They effectively improved the interlayer spacing, ion intercalation dynamics, electronic conductivity and structural stability of V_2O_5-based composite materials, thus enhanced the electrochemical performance. The pre-intercalation Cu to V_2O_5 (CuVO-300) exhibits excellent performance and can support the small lamp panel lighting (Fig. 5g). Chen et al. [100] developed a high-voltage, long-life zinc-vanadium bronze battery using $Co_{0.247}V_2O_5{\cdot}0.944H_2O$ nanoribbons. The high crystal structure can realize fast and reversible Zn^{2+} intercalation/deintercalation under high working voltage. Structural water acts as a pillar to stabilize the cathode structure during the intercalation and delamination of Zn^{2+}. In addition, the developed battery also shows high rate capability and long life over 7500 cycles, with a capacity retention rate of 90.26%. This research represents a significant progress in vanadium materials in various battery applications, achieving high discharge voltage and high capacity. Li et al. [101] prepared $Ag_{0.333}V_2O_5@V_2O_5{\cdot}nH_2O$ coaxial nano cables compact electrode for ZIBs (Fig. 5h). The 0.72 nm lattice fringe spacing points to (200) lattice plane of $Ag_{0.333}V_2O_5$. There is an amorphous $V_2O_5{\cdot}nH_2O$ layer of about 8 nm on the edge of the coaxial nanocrystal. This electrochemically stable structure is conducive to ion contact and penetration in electrodes, thus improving the storage performance of zinc ions. It is mainly due to its optimized ion/electron percolation and robustness of coaxial nanostructures.

3.5. $M_XV_3O_8$

Cation pre-intercalation to increase interlayer spacing is a useful method to enhance the electrochemical performance of aqueous ZIBs electrode materials. Another type of vanadate $M_xV_3O_8$ (M = H, Li, Na) is also an auspicious electrode material, which has also been extensively studied [32,102]. Sun et al. [103] examined the feasibility of electrochemical zinc ion intercalation into LiV_3O_8 and the corresponding progressive single-phase transition phase storage mechanism (Fig. 6a). This plate-like LiV_3O_8 exhibits high average discharge capacity. As shown in Fig. 6b, there are two distinct pairs of redox peaks appearing. Assign them to the two-step zinc intercalation/de-intercalation reaction process from LiV_3O_8 host. Generally, the large layer spacing of $Na_xV_3O_8$ is favourable for ion intercalation/de-intercalation. Mai et al. [104] developed a durable ZIBs system with $Na_2V_6O_{16}{\cdot}1.63H_2O$ nanowires cathode, and $Zn(CF_3SO_3)_2$ electrolyte. When cycling at 50 mA g^{-1}, the specific capacity of $Na_2V_6O_{16}{\cdot}1.63H_2O$ nanowires is as high as 352 mAh g^{-1}, and retention capacity is up to 90% after 6000 cycles at 5000 mA g^{-1}. The cycle performance is significantly improved compared to NaV_3O_8 nanowires. Fig. 6c reveals inherent Zn^{2+} storage mechanism. In the first discharge process, water molecules and Zn^{2+} are intercalated simultaneously. In the subsequent charging and discharging process, Zn^{2+} is reversibly intercalated into and from $Na_2V_6O_{16}{\cdot}1.63H_2O$ nanowires electrode. By the excellent electrochemical performance, good stability, more cost advantages and

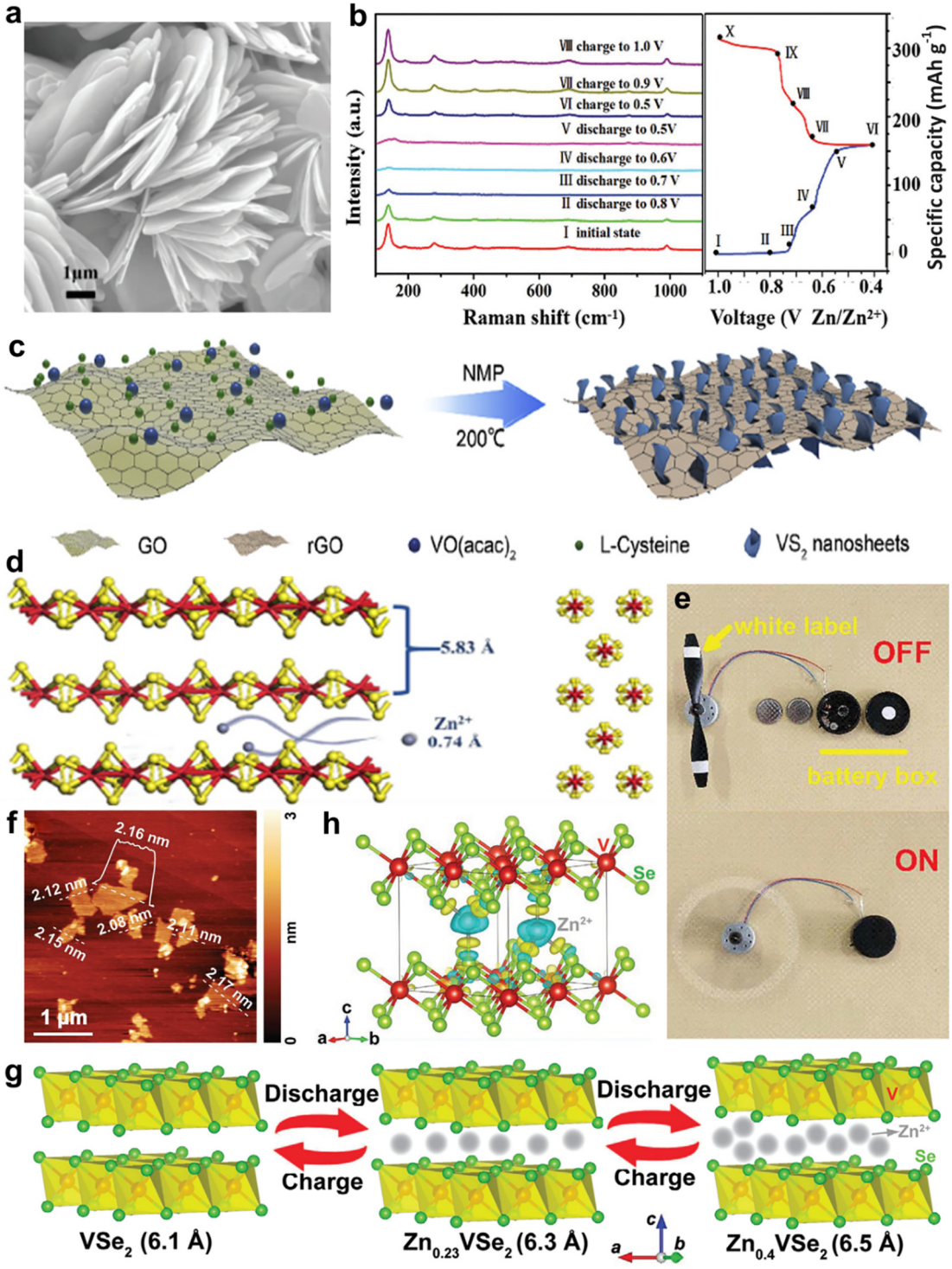

Fig. 8. (a) SEM image of layered VS_2, (b) In-situ Raman spectra of VS_2 electrode at a scan rate of 2.0 mV s^{-1} in the voltage range of 0.4–1.0 V. Reproduced from Ref. [125] with permission from Wiley-VCH. (c) Illustration of fabrication procedure of hierarchical rGO-VS_2 composites [126]. (d) Lateral (left) and vertical (right) views of the crystalline structure of VS_4. Reproduced from Ref. [127] with permission from Royal Society of Chemistry. (e) Two Zn//VS_4@rGO cells in series powering a mini motor with a fan. Reproduced from Ref. [128] with permission from Royal Society of Chemistry. (f) AFM image of the as-prepared VSe_2 nanosheets, (g) Schematic illustration of the two-step Zn^{2+} intercalation/deintercalation process in VSe_2 cathode, (h) The schematic illustration of charge density map after zinc-ion intercalation into the layered VSe_2 framework (yellow: charge increase; blue: charge decrease). Reproduced from Ref. [130] with permission from Wiley-VCH.

excellent safety performance, $Na_2V_6O_{16}{\cdot}1.63H_2O$ can be used as a reliable cathode material in aqueous ZIBs. Liang et al. [105] proposed a new preparation method, combining surface hydrotherapy reaction and freeze-drying technology to produce graphene film-coated $Na_{1.1}V_3O_{7.9}$ nanowires (Fig. 6d). This compound provides improved conductivity and capability to buffer changes in volume and stress during charge/discharge. This cathode has been used in aqueous sodium and zinc ion batteries, exhibiting good electro-

chemical performance. Outstanding electrochemical performance is due to the stable channel of layered $Na_{1.1}V_3O_{7.9}$ (Fig. 6e) and improved electrical conductivity from graphene film.

$H_2V_3O_8$ (or $V_3O_7{\cdot}H_2O$) possesses excellent lithium storage performance, and is popular in lithium-ion batteries [106]. It consists of V_3O_8 layer (composed of VO_5 trigonal bipyramid and VO_6 octahedron) bonded together by hydrogen bonding [107,108]. This layer structure provides a channel for the simple intercalation of multivalent Zn ions into $H_2V_3O_8$. The hydrogen bonding in $H_2V_3O_8$ helps to maintain the structural integrity and stability during charge and discharge, which is better than other layered vanadium oxides. $H_2V_3O_8$ also has a higher electronic conductivity, which is caused by the mixed-valence states of V^{5+} and V^{4+}. At the same time, the high average valence state (4.67) contributes to a larger specific capacity and more active redox sites [109]. Yan et al. [110] synthesized $H_2V_3O_8$ nanowire and built a Zn//Zn $(CF_3SO_3)_2$//$H_2V_3O_8$ battery. The sample exhibits high crystallinity and good electrochemical performance. Benefit from layered structure of $H_2V_3O_8$, the changes in the structure during intercalation/de-intercalation of zinc ions is slight. When discharged to 0.2 V, a characteristic peak of Zn appears in the XPS spectrum (Fig. 6f), which reveals that Zn^{2+} are inserted into the $H_2V_3O_8$ layered structure. The peak intensity of V^{5+} decreases, and peak intensity of V^{4+} increases, reflecting that with the insertion of Zn^{2+}, V^{5+} is reduced to V^{4+} (Fig. 6g). The battery delivers high discharge capacity of 423.8 mAh g^{-1} at 0.1 A g^{-1}. Wang et al. [111] developed $H_2V_3O_8$ nanowire/graphene composite material as a cathode in ZIBs. Density functional theory calculations manifest that intercalated zinc ions are stable at the centre of the vacant site (Fig. 6h). Zinc ion storage capacity of compounds is good, delivering long cycle stability (capacity retention of 87% over 2000 cycles at 20C) and excellent specific capacity (394 mAh g^{-1} at 1/3C, 270 mAh g^{-1} at 20C). The graphene sheets possess high specific surface area. It has a positive influence on optimizing charge transport property of composites. Therefore, it can improve electrode electrochemical kinetics and achieve fast and reversible intercalation/deintercalation of Zn^{2+}.

3.6. $M_3V_2(PO_4)_3$

In the crystal structure of NASICON vanadium phosphate (the basic form is $M_3V_2(PO_4)_3$, M = Li, Na), two [VO_6] octahedrons and three [PO_4] tetrahedrons share the vertex O atom. Thus, it connects and forms a [$V_2(PO_4)_3$] structural unit. Then it connects with other [$V_2(PO_4)_3$] through [PO_4] to create an open three-dimensional framework which can provide stable sites and ion migration channels. In the past decades, polyanion compounds have extensive diffusion channels for lithium ions and sodium ions, so they have been widely studied as electrode materials in both non-aqueous/aqueous lithium or sodium-ion batteries [112-114]. $Na_3V_2(PO_4)_3$ and $Li_3V_2(PO_4)_3$ own the Na superionic conductor (NASICON) structure. They are also used in ZIBs [115,116]. Zhou et al. [117] prepared reduced graphene oxide modified $Na_3V_2(PO_4)_3$ (NVP@rGO) microspheres through spray drying. HRTEM image shows the lattice fringes of $Na_3V_2(PO_4)_3$ intuitively, and (113) crystal plane spacing is 0.37 nm. Besides, at the edge of the microsphere, there is the thin amorphous rGO layer. The schematic illustration (Fig. 7a) and in-situ XPS results (Fig. 7b and c) clearly illustrate the co-intercalated of Zn^{2+} and Na^+ in $Na_3V_2(PO_4)_3$ frame during subsequent charge and discharge cycling. Check Zn and Na at the same time when discharged to 0.6 V. NASICON structured $Na_3V_2(PO_4)_3$ showed simultaneous Na^+/Zn^{2+} intercalation/de-intercalation in 2 M $Zn(CF_3SO_3)_2$ electrolyte, and delivered high specific discharge capacity. Huang and co-workers [118] developed one type of hybrid aqueous rechargeable battery with Zn metal as anode, $Na_3V_2(PO_4)_3$ as cathode and $Zn(CH_3COO)_2/CH_3COONa$ hybrid solution as the electrolyte. $Na_3V_2(PO_4)_3$ is co-incorporated by reduced graphene oxide and carbon (C-G-NVP). Fig. 7d shows the cycling property at 0.5C (0.8–1.7 V). This battery delivers a capacity of 92 mAh g^{-1} with flat and high operating voltage of 1.42 V. The total energy density of the battery can achieve approximately 112 Wh kg^{-1}, higher than other reported aqueous batteries (Fig. 7e).

Ion doping is also used in the modification of $Na_3V_2(PO_4)_3$. Mason et al. [119] proposed the idea of stabilizing $Na_3V_2(PO_4)_3$ with titanium, and studied the application of this material in aqueous sodium and zinc ion batteries. The as-prepared material demonstrates good cycling stability in the neutral sodium-containing electrolyte, while inferior in the zinc-containing electrolyte. Besides, $Na_3V_2(PO_4)_2F_3$ also can be applied as positive electrode material for ZIBs [120]. The crystal structure is bridged by the [VO_6] octahedron and [PO_4] tetrahedron through the common O/F atoms. Thus, stack into a unique three-dimensional tunnel structure. PO_4^{3-} and F^- with strong inductive effect improve the stability of the crystal structure and the working voltage, which is more conducive to the transmission and storage of Zn^{2+}.

3.7. VS_x

Layered transition-metal dichalcogenides have also attracted extensive attention from researchers in various fields because of its excellent characteristics of the graphene-like layered structure and rapid ion diffusion [121]. VS_2 has great potential in the intercalation/de-intercalation of ions (Li, Na, Zn, Mg, Al) due to its large interlayer distance [122-124]. As shown in Fig. 8a, Mai et al. [125] fabricated VS_2 flower assembled from nanosheets with a thickness of 50–100 nm. The interlayer spacing of VS_2 can well accommodate the intercalated Zn ions, which plays a pivotal effect in achieving long-life ZIBs. In-situ Raman spectra of VS_2 at different working potentials are shown in Fig. 8b. During the discharge process, the bonds become broader and weaker due to the Zn^{2+} intercalation into the layers of VS_2. It reversibly returns to the original state after charging. This material exhibits good cycling stability and high capacity. The Coulombic efficiencies approach to 100% in all cycles. Initial discharge capacity is 112.3 mAh g^{-1} at 0.5 A g^{-1}, and it maintains 110.9 mAh g^{-1} after 200 cycles. Fan et al. [126] successfully grew ultra-thin VS_2 nanosheets on the surface of the graphene sheet through one-step solvothermal method (Fig. 8c). This 2D hierarchical composite combines the synergistic advantages of VS_2 nanosheets and graphene sheet to show excellent performance.

Vanadium tetrasulfide (VS_4) is reported to owned unique one-dimensional atomic-chain structure and used in ZIBs as an intercalation-type cathode. Yu et al. [127] confirmed that VS_4 stored energy through the zinc ion intercalation mechanism. The atomic chain interval is 5.83 Å (Fig. 8d), which is much larger than the diameter of zinc ions (0.74 Å). Besides, Yang et al. [128] introduced graphene with excellent electrical conductivity into VS_4 by hydrothermal method and proposed an intercalation and conversion mechanism. And powering the micro electric fan visually demonstrates the practical application of this battery (Fig. 8e).

In addition to the layered transitional metal dichalcogenide VS_2, VSe_2 can also be used as electrode material for ZIBs. Two selenium layer and one vanadium layer are alternately distributed in VSe_2 layered structure and connected by van der Waals force interaction. The interlayer spacing is as large as 6.11 Å. The neighbouring V^{4+}-V^{4+} generate electron coupling force between, make the material possess excellent electronic conductivity and metallic character, and suitable as electrode material [129]. Hu et al. [130] reported ultra-thin VSe_2 nanosheets with a lateral size of 1 μm and average thickness of 2.1 nm (Fig. 8f). Fig. 8g shows the intercalation and dis-intercalation of zinc ions in the VSe_2 sample during the charge and discharge process. DFT calculation confirms the charge redistribution after Zn^{2+} insertion in VSe_2 layered frame-

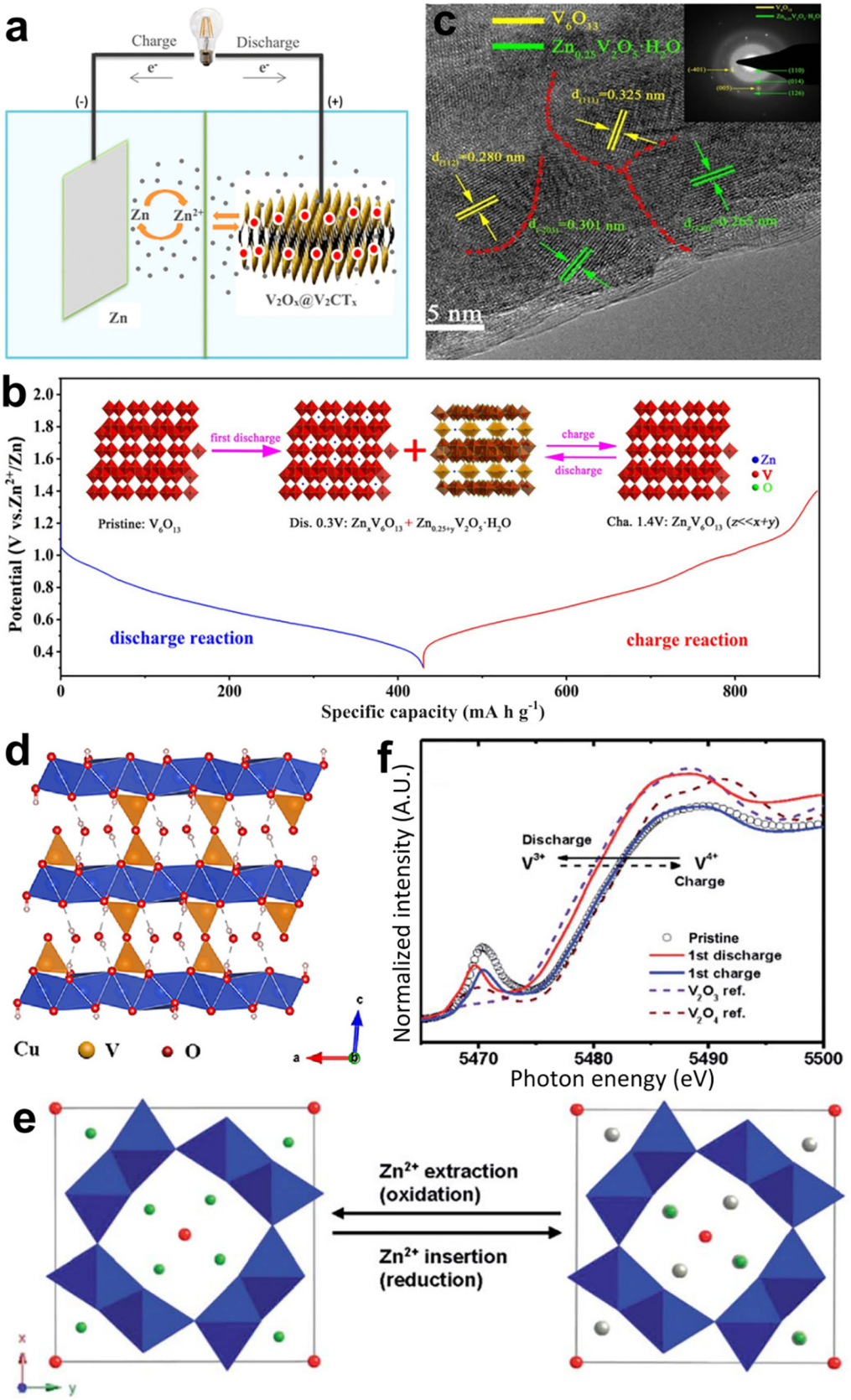

Fig. 9. (a) Schematic illustration of the Zn//V_2O_x@V_2CT_x MXene battery configuration with 1 M $ZnSO_4$ aqueous electrolyte. Reproduced from Ref. [132] with permission from American Chemical Society. (b) Schematic illustration of highly reversible phase transition during discharge–charge process of V_6O_{13}, (c) HRTEM image with corresponding SAED pattern at fully discharged state. Reproduced from Ref. [137] with permission from Wiley-VCH. (d) Crystal structure of $Cu_3V_2O_7(OH)_2{\cdot}2H_2O$ [133]. (e) Zn^{2+} intercalation/deintercalation into/out of the $VO_{1.52}(OH)_{0.77}$ and Al-doped $VO_{1.52}(OH)_{0.77}$ tunnel model structure, (f) K-edge XANES spectra obtained during discharging and charging. Reproduced from Ref. [140] with permission from Royal Society of Chemistry.

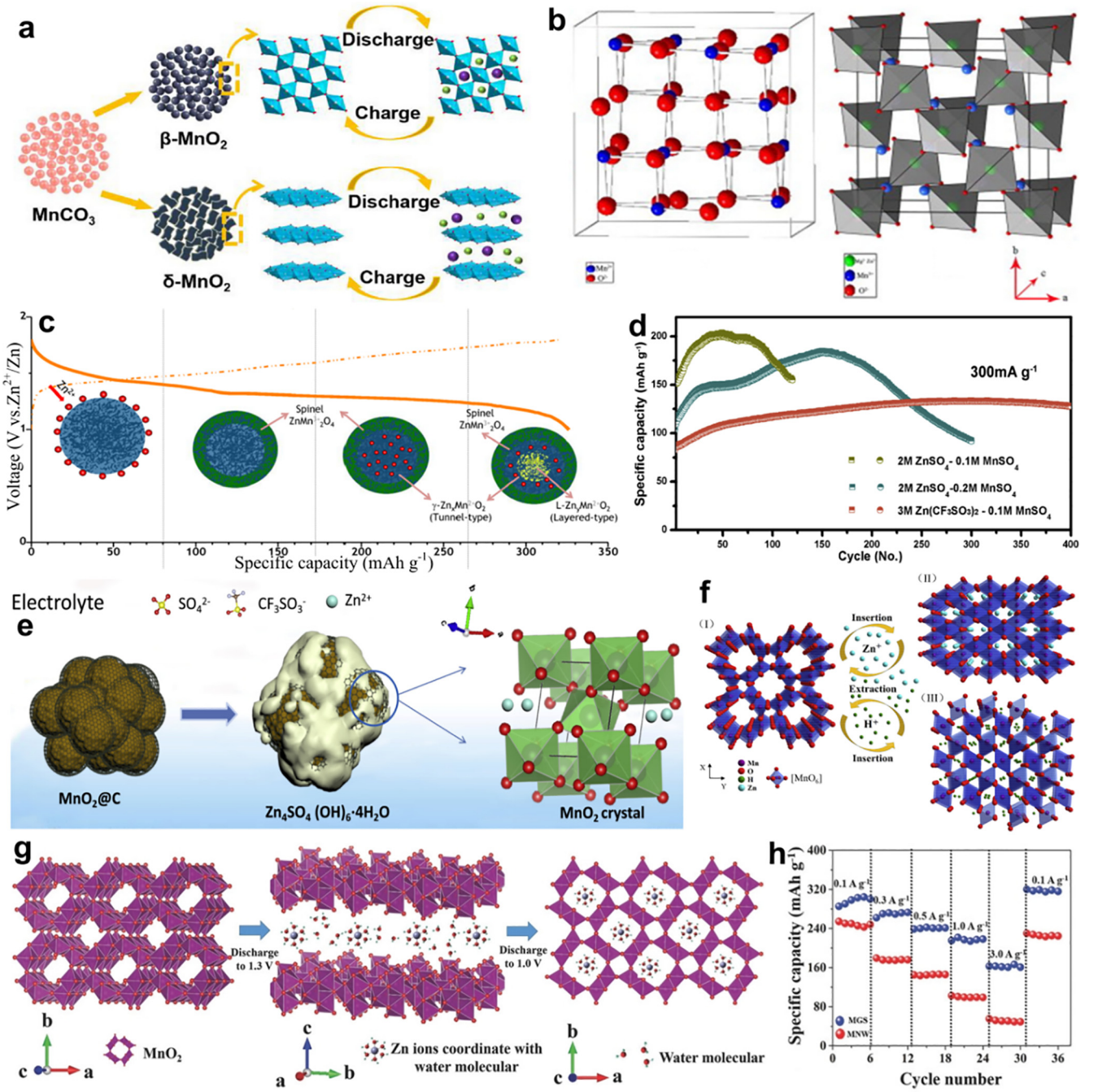

Fig. 10. (a) Schematic sketch of the synthesis of β-MnO_2 and δ-MnO_2 submicrospheres [150]. (b) Cubical structure λ-MnO_2 with void spaces and MMn_2O_4 (M = Mg, Zn) after the intercalation of M^{2+} [46]. (c) Schematic illustration of the reaction pathway of Zn-insertion in the prepared γ-MnO_2 cathode. Reproduced from Ref. [151] with permission from American Chemical Society. (d) Cycle performance of β-MnO_2@C with 2 M $ZnSO_4$-0.1 M $MnSO_4$, 2 M $ZnSO_4$-0.2 M $MnSO_4$ and 3 M $Zn(CF_3SO_3)_2$–0.1 M $MnSO_4$, (e) Schematic showing the reactions during the discharge process for β-MnO_2//Zn cell employing the aqueous 3 M $Zn(CF_3SO_3)_2$–0.1 M $MnSO_4$ electrolyte [155]. (f) Schematic illustration of the intercalation mechanism of α-MnO_2/CNT microspheres-based ZIBs at 0.2 A g^{-1}, voltage cutoffs of 1.2–1.85 V: (I) α-MnO_2, (II) $ZnMn_2O_4$, (III) MnOOH [158]. (g) Schematic illustration of the two-step intercalation mechanism of MGS cathode, (h) Rate performances of MGS and MNW cathodes. Reproduced from Ref. [159] with permission from Wiley-VCH.

work (Fig. 8h). Charge around part of V and Se increases, while charge around Zn reduced greatly, implying that ligand Se anion bonds with the intercalated Zn.

3.8. Other vanadium-based materials

On the way to develop cathode materials, good cycling performance and high capacity are the two important parameters. Except for the above electrode materials, there are other vanadium-based materials used in aqueous ZIBs, such as VN_xO_y [131], V-based MXenes [132], $Cu_3V_2O_7(OH)_2{\cdot}2H_2O$ [133], $Zn_2V_2O_7$ [134], V_3O_7 [135,136], V_6O_{13} [137], $Na_5V_{12}O_{32}$ [138], $K_2V_8O_{21}$ [138], $(NH_4)_2V_{10}O_{25}{\cdot}8H_2O$ [138,139], $VO_{1.52}(OH)_{0.77}$ [140], $NH_4V_4O_{10}$ [141], $Ba_{1.2}V_6O_{16}{\cdot}3H_2O$ [142].

Recently, Zhou et al. [131] discovered an innovative energy storage mechanism in Zn/VN_xO_y battery system in which anionic (N^{3-}/N^{2-}) and cationic (V^{3+}/V^{2+}) redox reactions co-occurred. The VN_xO_y electrode presents high reversibility and little structural degradation, and the battery delivers high cycling stability and superior rate capability.

Two-dimensional layered transition metal nitrides and carbides (MXenes) is developing as an ideal energy storage electrode because of its rich chemical variables and ion intercalation structure. V_2CT_x MXenes are commonly applied in lithium-sulfur batteries and lithium-ion batteries, and V_2C MXene can be used as cathode aqueous zinc-ion hybrid supercapacitor [143]. Qin et al. [132] also reported the application of vanadium carbide MXene in ZIBs. V_2O_x on two dimensional V_2CT_x can be formed by high-temperature etching, and V_2O_x@V_2CT_x could serve as high rate performance cathode (Fig. 9a).

V_6O_{13} with mixed V valences (V^{4+}/V^{5+}) has an inherent open structure, benefiting to the improvement of electronic conductivity and rapid diffusion of Zn ions. The excellent characteristics are promising to solve the problem of a sharp drop in the capacity of VO_2 and V_2O_5 electrodes due to low electron conductivity and poor structural reversibility. Liang et al. [137] found that V_6O_{13} ultrathin nanosheet showed excellent Zn storage performance due to the shortened ion diffusion distance and large contact area. As seen in Fig. 9b, zinc ions reversibly intercalate into/de-intercalate from V_6O_{13} lattice framework. At the fully discharged state, HRTEM image and the corresponding SAED pattern (Fig. 9c) shows the V_6O_{13} and $Zn_{0.25}V_2O_5{\cdot}H_2O$ phases distinctly. This V_6O_{13} exhibits high capacity and good long-term cycling stability (206 mAh g^{-1} at 10 A g^{-1} over 3000 cycles). Structured water can be used as a pillar of layered V_6O_{13} to enhance the cycle stability and rate capability. These pillars can provide a fast Zn^{2+} diffusion channel and effectively improve the structural stability during charge and discharge. Wang et al. [59] developed a novel hydrated $V_6O_{13}{\cdot}nH_2O$ as promising cathode. The electrochemical performance of $V_6O_{13}{\cdot}nH_2O$ is greatly enhanced, and it has great potential for large-scale practical ZIB applications.

$Cu_3V_2O_7(OH)_2{\cdot}2H_2O$ is one type of layered structure copper vanadate mineral. Its crystal structure is made up of $Cu_3O_6(OH)_2$ layers separated by unligated water molecules and V_2O_7 pillars (Fig. 9d). The insertion of zinc ions into the crystal lattice to replace copper will cause a phase change. In the subsequent chemical reaction, zinc ions are reversibly inserted and extracted in the new $Zn_3(OH)_2V_2O_7{\cdot}2H_2O$ phase. It is a new mechanism, including phase transition and Zn^{2+} intercalation/de-intercalation. Zhou et al. [138] studied the electrochemical property of $(NH_4)_2V_{10}O_{25}{\cdot}8H_2O$ in ZIBs. They compared that with V_2O_5, $Na_5V_{12}O_{32}$, and $K_2V_8O_{21}$. $(NH_4)_2V_{10}O_{25}{\cdot}8H_2O$ possesses a stable double-layer structure. The introduction of cations into the V_2O_5 framework can improve the ionic conductivity of Zn, and rearrange the vanadium oxygen structural units. Structural unit rearranged vanadate has a significant improvement in rate discharge capacity, cycle stability, and energy density. For example, the capacity of $(NH_4)_2V_{10}O_{25}{\cdot}8H_2O$ is much higher than other electrode materials at 5 A g^{-1}.

Furthermore, Myung et al. [140] firstly developed $VO_{1.52}(OH)_{0.77}$ and Al-doped $VO_{1.52}(OH)_{0.77}$ for aqueous ZIBs as electrode candidate. Al ions are successfully incorporated into hollandite $VO_{1.52}(OH)_{0.77}$ tunnel structure. The Zn^{2+} intercalation/de-intercalation electrochemical reaction model in tunnel structure of $VO_{1.52}(OH)_{0.77}$ composite is displayed in Fig. 9e. The XANES spectrum reveals that vanadium is reduced to +3 valence when discharging and oxidized to +4 valence when charging (Fig. 9f). Because of its strong Al-O bond with the stable crystal structure, its capacity and retention rate significantly increase. Electrode materials for ZIBs are developing rapidly and deserve more extensive research.

4. Manganese-based cathode materials

The earth's crust is rich in manganese resources. Manganese-based compounds are popular in desulfurizers, catalysts, battery electrode materials, and steel-making deoxidizers [144,145]. And manganese has the unique advantages of multivalent states (Mn^{2+}, Mn^{3+}, Mn^{4+}, Mn^{7+}). Manganese-based compounds exhibit significant atomic structure diversity and multivalent phases [32]. Many high-quality structures can easily accommodate various metal cations, including zinc ions. It also owes advantages of high operating voltage, environmental friendliness, low toxicity, and low cost [146]. Manganese-based compounds include MnO_2, Mn_2O_3, Mn_3O_4, $ZnMn_2O_4$, $LiMn_2O_4$, some of which are considered as promising cathode materials in aqueous ZIBs.

4.1. MnO_2

At the early stage of developing rechargeable ZIBs, as a representative energy storage material, MnO_2 has received extensive attention due to its large natural abundance, structural tunability and high Zn storage properties [147]. Layered or tunnel structure of MnO_2 can reversibly intercalate/de-intercalate Zn ions [148]. As we all know, the zinc storage ability of ZIBs with MnO_2 as cathode depends on MnO_2's crystal structure to a great extent. It can be prepared under different reaction conditions [25]. The basic crystal structure of MnO_2 is an [MnO_6] octahedral unit that is coordinated by one manganese atom and six oxygen atoms. Adjacent octahedral units share the edges and corners to connect, forming a complex tunnel structure network. The MnO_2 material family has a variety of crystallographic polymorphisms, which is classified according to the type of connection between the basic octahedral units [MnO_6] [149]. The basic structural unit of [MnO_6] octahedron can be assembled into a layer/tunnel/chain structure through sharing corners and sides, thereby forming varieties of different MnO_2 crystal structure. The typical crystal structures of MnO_2 include λ-MnO_2, α-MnO_2, β-MnO_2, γ-MnO_2, δ-MnO_2, R-MnO_2, todorokite-MnO_2 [26,53].

Various crystal forms of MnO_2 have applications in ZIBs as cathode materials. δ-MnO_2 and β-MnO_2 were synthesized with $MnCO_3$ submicrospheres as precursors, as illustrated in Fig. 10a [150]. They are composed of nanosheets and nanoparticles. As cathode, 99% and 81% of the initial capacity are maintained for β-MnO_2 and δ-MnO_2 at a current density of 100 mA g^{-1} after 100 cycles. Also, due to the larger layer spacing of δ-MnO_2, it is conducive to ion insertion/extraction. β-MnO_2 possesses stable 3D tunnel structure, thus shows better cycle stability than δ-MnO_2. Cao et al. [46] produced λ-MnO_2 with cubical structure, which can intercalate polyvalent cations (Zn^{2+}, Mg^{2+}) in aqueous electrolyte (Fig. 10b). It displays ideal intercalation/de-intercalation performance as the cathode. Kim et al. [151] researched the electrochemical property of γ-MnO_2 in 1 mol L^{-1} $ZnSO_4$ electrolyte. As shown in Fig. 10c, tunnel-type MnO_2 undergoes the structural transformation into a spinel-type $ZnMn_2O_4$, when the zinc ions are fully intercalated. The charge and discharge curves show a defined platform at approximately 1.25 V vs Zn/Zn^{2+}. Liang et al. [152] used the pre-intercalation method of sodium ions and water molecules to stabilize the δ-MnO_2 layered structure and activate the stable zinc ion storage of δ-MnO_2. The results show that the prepared zinc//pre-intercalation δ-MnO_2 battery has extremely high rate performance. Due to the smooth diffusion of zinc ions in the pre-intercalation structure, the capacity retention rate after 10,000 cycles of charge and discharge is as high as 98%.

MnO_2 suffers from severe capacity decay at high current density in mild aqueous electrolytes [153]. The carbon material is a cyclic compatible material, which can greatly improve electrical conductivity and mechanical elasticity, and ease the volume change [154]. β-MnO_2@C mixed sample was synthesized via plasma-assisted milling as cathode material [155] where MnO_2 nano crystallites were wrapped and combined with a thin carbon layer obtained from expanding graphite. In 0.1 M $MnSO_4$-3 M $Zn(CF_3SO_3)_2$

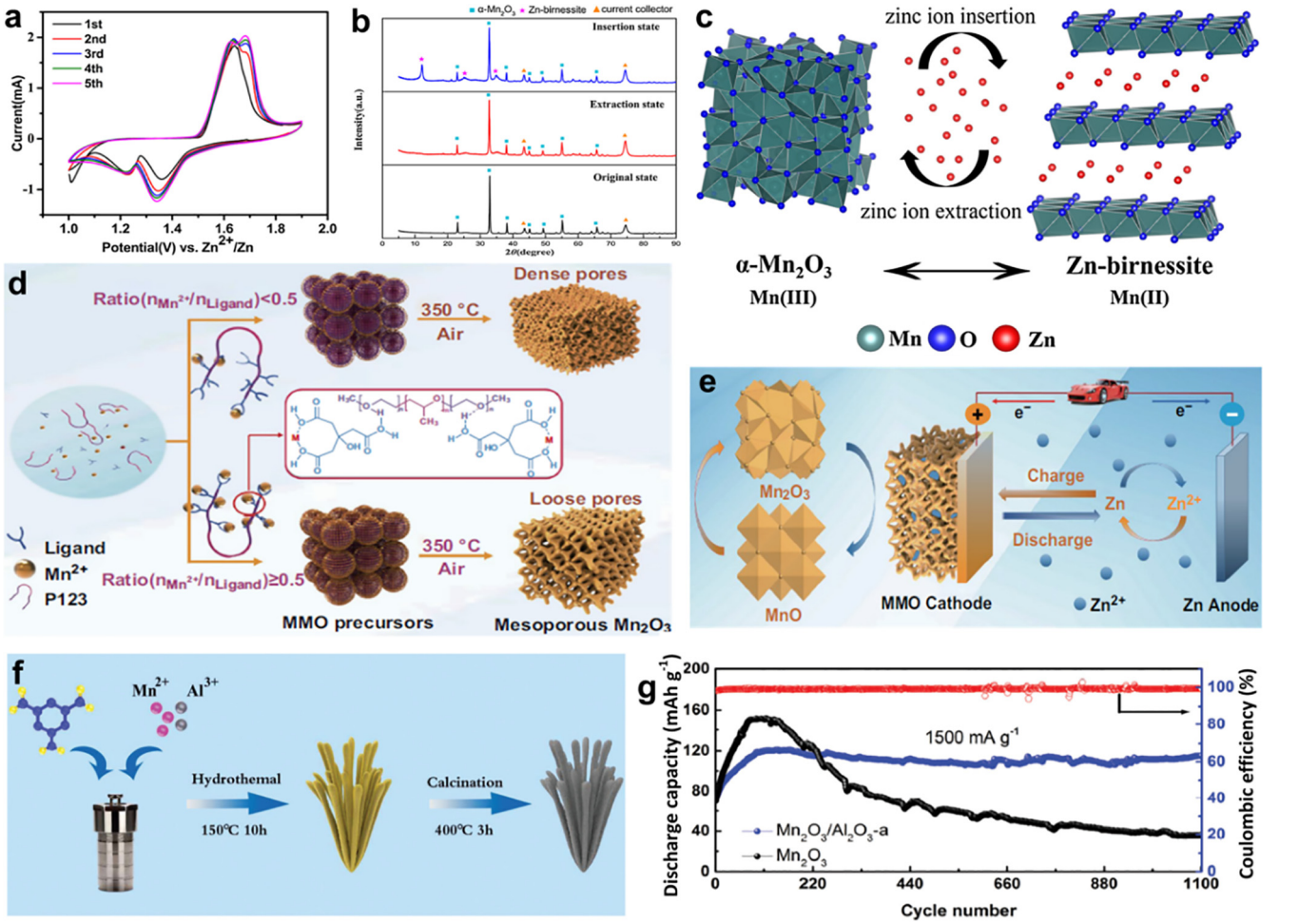

Fig. 11. (a) CV curve of battery at 0.5 mV s^{-1}, (b) XRD patterns of α-Mn_2O_3 cathode at original state, zinc ion extraction state and zinc ion insertion state, (c) Schematics of α-Mn_2O_3 as cathode material for zinc ion battery [166]. (d) Schematic illustration of the formation process for mesoporous Mn_2O_3, (e) Illustration of charge/discharge process for Zn/Mn_2O_3 aqueous rechargeable battery. Reproduced from Ref. [169] with permission from Springer Nature. (f) Schematic illustration of the formation of the Mn_2O_3/Al_2O_3 composite, (g) The long-term cycling performance of the Mn_2O_3 and Mn_2O_3/Al_2O_3 electrodes at a high current density of 1500 mA g^{-1}. Reproduced from Ref. [170] with permission from Royal Society of Chemistry.

electrolyte, this hybrid presents good cycle stability with a high capacity of 130 mAh g^{-1} after 400 cycles at 300 mA g^{-1} (Fig. 10d). The pores of β-MnO_2@C particles promote electrolyte penetration effectively. The combination with carbon effectively helps to alleviate the dissolution of MnO_2 and improves the conductivity of the sample (Fig. 10e). Kong et al. [156] grew the MnO_2 nanoparticles on the surface of N-doped hollow porous carbon nanosphere. Owing to the unique structure of the carbon microspheres and MnO_2 composite, this electrode exhibits excellent zinc storage performance.

It is noted that conductive additives and binders are commonly used for most electrodes. Carbon nanotubes and graphene can form conductive networks due to their flexibility, stability and high conductivity [157]. Chi and co-workers [158] developed α-MnO_2 nanofibers/carbon nanotube microspheres as the cathode by a chemical precipitation/spray granulation combination method. A unique hierarchically assembled microspheres structure is formed by this strategy. Due to the synergistic advantage of structural properties of α-MnO_2 nanofibers and highly conductive carbon nanotube network, the areal energy density and charge transfer dynamics greatly increased. After activation, the insertions of H^+ and Zn^{2+} are reversible in one-dimensional 2 × 2 and 1 × 1 tunnels (Fig. 10f). It is worth noting that the battery displays superior cycle durability with the high capacity retention of 96% after 10,000 cycles at 3 A g^{-1}. Graphene scroll coating α-MnO_2 nanowire (MGS) was also employed [159]. The conductivity of MGS is increased greatly by graphene, and the dissolution of cathode materials is alleviated. Zinc ions form Zn-buserite combined with water molecules, and then deeply insert into α-MnO_2 (Fig. 10g). Compared with the bare α-MnO_2 nanowire (MNW), the rate performance is significantly improved (Fig. 10h). Besides, Lu et al. [160] composed γ-MnO_2 nanorods with highly conductive graphene. Its electrochemical performance is significantly improved because graphene could enhance the conductivity and protect the electrode structure.

Besides, the introduction of metal ions (Na^+, K^+, Ca^{2+}, Ba^{2+}, Zn^{2+}, La^{3+}) into manganese oxide to form manganate can also improve the electrochemical performance of ZIBs [61,161,162]. Peng et al. [163] reported δ-MnO_2 nanoflake with Na+ intercalation served as the cathode. The insertion of Na^+ into the interlayer of the matrix material enhances ionic conductivity and promotes electrochemical kinetics. Liu et al. [164] found that the pre-intercalated of K^+ stabilizes the MnO_2 structure, and promotes the Zn^{2+} diffusion. Lu et al. [162] proposed La^{3+} and Ca^{2+} co-doped MnO_2 by one-step liquid coprecipitation method. Ca^{2+} mainly improves stability, and both Ca^{2+} and La^{3+} affect the enhancement of capacity and reversibility.

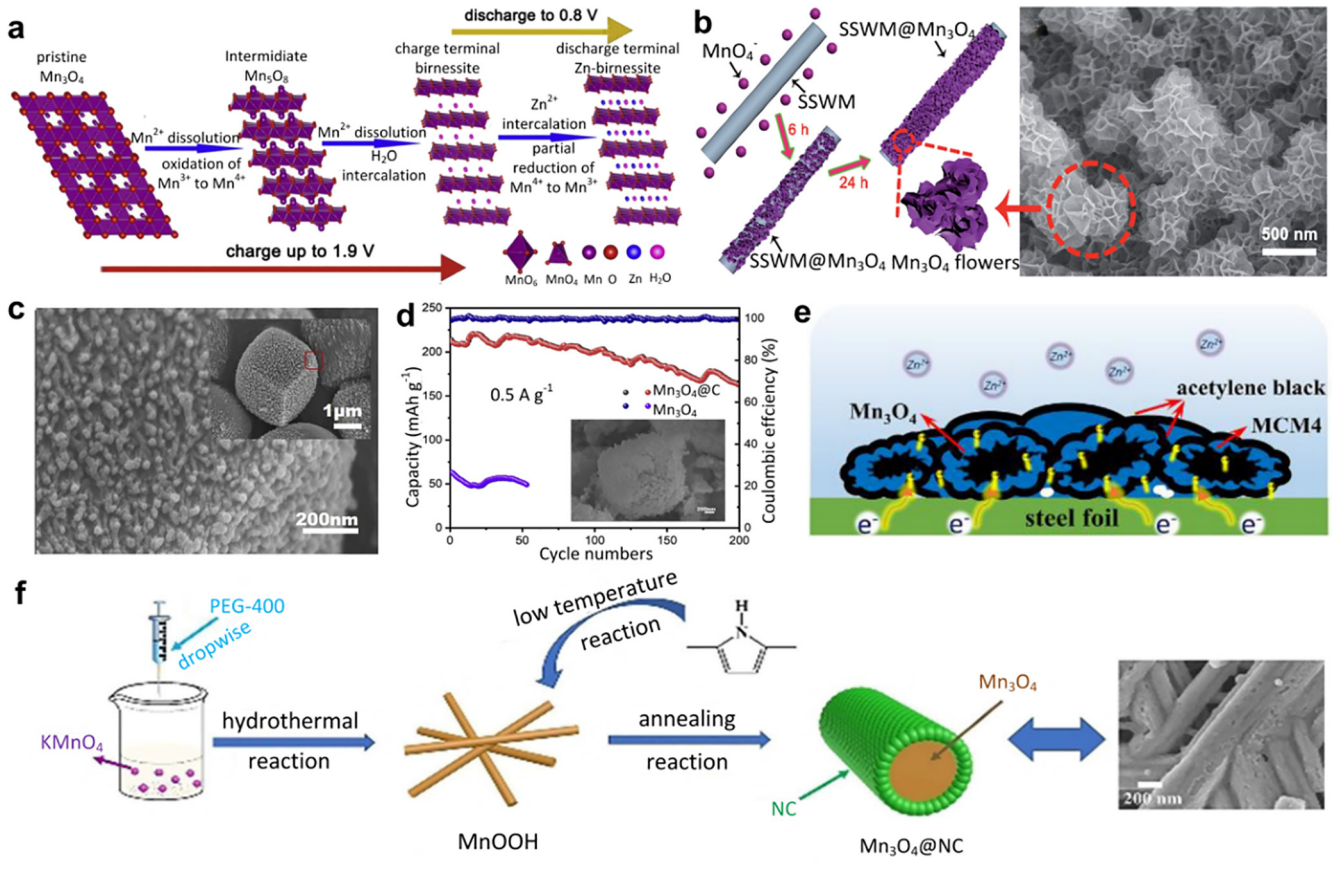

Fig. 12. (a) Schematic of reaction pathway within the first cycle [172]. (b) Synthesis schematic and SEM image of Mn_3O_4. Reproduced from Ref. [173] with permission from Royal Society of Chemistry. (c) SEM image of Mn_3O_4@C, (d) Cycling performance of Mn_3O_4@C (inset: SEM images after cycling) [177]. (e) Schematic diagram of electronic transmission on MCM4@Mn_3O_4 electrodes [178]. (f) Schematic illustration of the synthesis of Mn_3O_4@NC. Reproduced from Ref. [179] with permission from Wiley-VCH.

In short, MnO_2 with various crystal structures has been studied for aqueous ZIBs as positive electrode materials, exhibiting unique characteristics of charge/discharge process and excellent electrochemical performance. However, there is still no consensus on the discussion of the specific reaction mechanism.

4.2. Mn_2O_3

Manganese oxides are the promising cathodes for rechargeable batteries because of its high safety and low price [165]. But the practical application of Mn_2O_3 in ZIBs is still puzzled due to its poor rate performance and low specific capacity. Kang et al. [166] first reported the zinc storage performance of manganese (III) oxide. Fig. 11a shows the cyclic voltammetry curves of Zn//$ZnSO_4$//Mn_2O_3 battery. As seen, the peaks at 1.23 and 1.34 V indicate that Zn^{2+} can be intercalated into two different sites of host electrode. And two gradually inclined plateaus of the charge–discharge curve can be observed at about 1.27 and 1.4 V, which also indicates that α-Mn_2O_3 cathode presents excellent zinc storage property. With the charging and discharging process of the battery, α-Mn_2O_3 undergoes the reversible phase transition process between layered-type zinc birnessite and bixbyite structure. New peaks at 12.2°, 25.3°, 35.0° appear when charging to 1.9 V, illustrating the appearance of zinc birnessite (Fig. 11b). Fig. 11c shows the zinc ions intercalation/de-intercalation behaviour. The study of zinc storage mechanism helps to broaden the understanding of electrochemical mechanism and behaviour of aqueous ZIBs.

Due to the inevitable change in volume, the specific capacity of Mn_2O_3 electrode is low. The construction of a porous structure is considered as an effective method to relieve expansion [167]. The porous structure can offer a shortcut for ion diffusion, and the increased surface area can provide more reaction sites between the electrolyte and active material [168]. These two aspects synergistically ensure the cycle stability and rate capability of the battery. Qiao et al. [169] obtained high crystallinity of nano porous Mn_2O_3 cathode with adjustable pore size. They adopted the ligand-assisted self-assembly process (Fig. 11d). Due to the introduction of nano porous electrode structure, Zn//Mn_2O_3 batteries display excellent rate capability and significant cycle durability. Besides, a mechanism for co-intercalation of H^+ and Zn^{2+} is also proposed. Zn^{2+} and H^+ are intercalated together to form a mixed metal oxide (MMO) cathode. Also, they can transform reversibly (Fig. 11e).

Dissolution of Mn^{2+} is a key problem for manganese-based cathodes. To alleviate this issue, Li et al. [170] synthesized a novel Mn_2O_3/Al_2O_3 composite material using MOFs as precursors by hydrothermal process and thermal decomposition (Fig. 11f). Many nanorods make up the micro bundle morphology. Al_2O_3 can effectively suppress the dissolution of Mn^{2+} from Mn^{3+} disproportionation. After compositing with Al_2O_3, the obtained material delivers higher capacity and better cycle stability. As shown in Fig. 11g, after 1100 cycles at 1500 mA g^{-1}, this composite has a discharge capacity of 118 mAh g^{-1}. The research results can provide some inspiration for modifying manganese-based materials in ZIBs and other battery systems.

4.3. Mn_3O_4

Only a few manganese oxides can be cathode materials for ZIBs [171]. Mn_3O_4 is an important one, in which the valence of

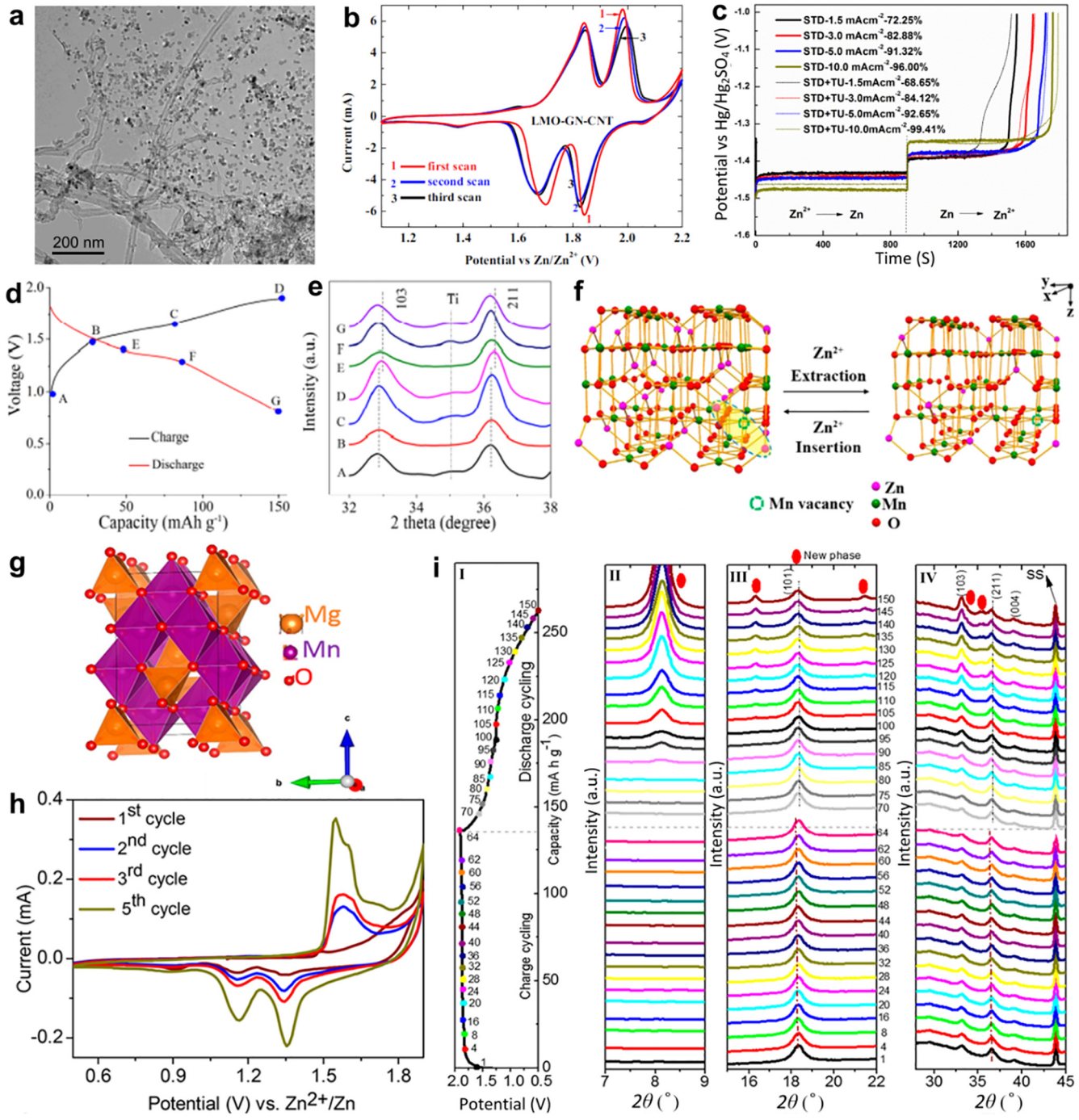

Fig. 13. (a) TEM image of LMO-GN-CNT composites, (b) CV curves of the LMO-GN-CNT electrode. Reproduced from Ref. [180] with permission from Springer Verlag. (c) The effect of current densities and different electrolytes of STD and STD + TU on the deposition/dissolution process of Zn-half cell [181]. (d) Charge/discharge curves (third cycle) of ZMO/C electrode at 50 mA g^{-1} in 3 M $Zn(CF_3SO_3)_2$ electrolyte, The points marked the states where data were collected for analysis, (e) Corresponding XRD patterns within selected angle (2θ) of 30-38°, (f) Schematic illustration of Zn^{2+} insertion/extraction in an extended three-dimensional ZMO spinel framework. Reproduced from Ref. [183] with permission from American Chemical Society. (g) The crystal structure of $MgMn_2O_4$, (h) CV patterns for $MgMn_2O_4$ in $MgSO_4$ + $ZnSO_4$ + 0.1 mol L^{-1} $MnSO_4$ electrolyte in the potential window of 0.5–1.9 V, (i) Electrochemical charge/discharge profile of the assembled electrochemical cell cycled within 1.9–0.5 V at 100 mA g^{-1}. The corresponding profile starts from scan no. 1 (open-circuit voltage) to scan no. 150 (0.5 V end of first discharge) (I). In-situ XRD patterns within selected scanning angle (2θ) domains of 7-9° (II), 15-22° (III), and 28-45° (IV). Reproduced from Ref. [184] with permission from American Chemical Society.

manganese is a mixture of two and three valences. This material is low in cost, abundant in resources, low in toxicity, and owns good compatibility in aqueous battery systems. Kang et al. [172] proved that Mn_3O_4 possessed excellent electrochemical performance in mild $ZnSO_4$ aqueous solution. The spinel Mn_3O_4 transforms into the Mn_5O_8 transition state, and then transforms to Zn-birnessite (Fig. 12a). Zhou et al. [173] reported flower-like Mn_3O_4 with high zinc storage capability (Fig. 12b). This Mn_3O_4 displays a lower electrode reaction resistance and a larger ion diffusion kinetics thanks to the binder-free conductive substrate, making it have excellent electrochemical performance.

However, massive volume change and low conductivity (10^{-7}-10^{-8} S cm^{-1}) of Mn_3O_4 during cycling seriously restrict application potential in energy storage and conversion devices [174]. The

design of nanostructures not only extends the contact area between electrode materials and electrolyte, but also shortens transmission distance of guest ions [175]. The introduction of carbon material in the electrode can enhance conductivity and reduce the electrode pulverization due to volume expansion during charging and discharging process [176]. Cubic Mn_3O_4@C materials with carbon layers and connecting pores were prepared through the one-step hydrothermal process [177]. This sample (Fig. 12c) has the advantages of protection of carbon layers, high conductivity, and high specific surface area. Fig. 12d presents Coulombic efficiency and cycling performance of Mn_3O_4@C materials. It remains a Coulombic efficiency of close to 100% throughout 200 cycles and high capacity retention of 77.1%. Liu's group [178] coated Mn_3O_4 particles on the surface of mesoporous carbon materials (MCM) made from litchi shell, which exhibited superior electrochemical performance as cathode for ZIBs. The effective combination of Mn_3O_4 and MCM is beneficial to improve ion transport and electronic conductivity (Fig. 12e). The reversibility and long-term cycle performance of the battery are significantly enhanced.

Heteroatom doping (such as N, S, and P) is beneficial for increasing the active sites quantity of carbon materials and is an efficient strategy to outshine electrochemical performance. Liu and co-workers [179] studied one novel Mn_3O_4@N-doped carbon matrix (Mn_3O_4@NC) cathode for ZIBs, using polypyrrole as nitrogen/carbon source and MnOOH nanorods as self-sacrifice template (Fig. 12f). The surface of Mn_3O_4 nanorods is evenly coated by 100 nm thick N-doped carbon layer. The high-resolution XPS spectrum for N 1 s showed the characteristic peaks of pyridinic, pyrrolic, and graphitic nitrogen. The electrode capacity decreased slightly and remained the specific capacity of 180 mAh g^{-1} after 500 cycles at 500 mA g^{-1}. While capacities increased in initial cycles as a result of activation. There is the synergistic effect of Mn^{2+} and Zn^{2+} from electrolyte and N-doped carbon shell. Benefiting from that, the Mn_3O_4 nanorods demonstrate good cycling stability.

4.4. $M_xMn_2O_4$

In addition to manganese oxide, manganate compounds $M_xMn_2O_4$ (M = Li, Na, Mg, Zn, etc) are also applied as positive electrode materials for ZIBs. Yuan et al. [180] synthesized $LiMn_2O_4$ cathode mixed with graphene and carbon nanotubes (LMO-GN-CNT) for rechargeable hybrid aqueous batteries (Fig. 13a). The electrolyte is 0.5 mol L^{-1} $LiCH_3COO$ and 0.5 mol L^{-1} $Zn(CH_3COO)_2$. Nano $LiMn_2O_4$ particles reveal good dispersibility. The addition of graphene and carbon nanotubes can improve the conductivity of the electrode, shorten diffusion length of electrolyte, and provide a large specific surface area, so it demonstrates excellent reversible electrochemical performance (Fig. 13b). To optimize the performance of Zn//$LiMn_2O_4$ aqueous batteries, Chen et al. [181] systematically studied the battery system using thiourea (TU) as electrolyte additive and polished industrial zinc foil as a current collector. The results prove that cycle performance and Coulombic efficiency of battery are significantly enhanced. Thiourea can be adsorbed on zinc anode collector surface, thereby improving the efficiency of the zinc deposition and dissolution (Fig. 13c). XRD and SEM results confirm that thiourea in the electrolyte has little effect on the crystal structure of $LiMn_2O_4$ electrode.

Inspired by the successful application of $LiMn_2O_4$, spinel $ZnMn_2O_4$ is also used as the electrode material of the battery. The spinel structure material is not suitable for intercalation of zinc ions. When the material contains defects (vacancies), the diffusion of zinc ions is easier due to the lower electrostatic repulsion [182]. The generation of defects in spinel materials opens up a new way for transport of divalent ions. Cheng and co-workers [183] reported cation-defective spinel $ZnMn_2O_4$ as Zn-insertion cathode. The efficiency of Zn^{2+} plating/stripping is about 100% in the 3 M $Zn(CF_3SO_3)_2$ solution, and it is stable for a long time. The highly reversible $ZnMn_2O_4$ spinel/carbon cathode (ZMO/C) material exhibits superior long term cycling capacity (94% retention after 500 cycles at 500 mA g^{-1}) and high specific discharge capacity (150 mAh g^{-1} at a rate of 50 mA g^{-1}). Fig. 13d and e display the representative galvanostatic charging/discharging curves and ex-situ XRD of points of ZMO/C at stabilized third cycle. During charge and discharge process, the expansion and shrinking of the crystal lattice are reversible. Zn^{2+} intercalation into and de-intercalation from Zn-O tetrahedron sites in ZMO spinel electrode (Fig. 13f). The research results have certain implications and promotion for development of the high-property rechargeable ZIBs using spinel compounds with cation defects.

Furthermore, Kim et al. [184] first constructed a new type of rechargeable aqueous metal-ion battery with zinc as the anode and spinels $MgMn_2O_4$ (Fig. 13g) as the cathode. Initial CV curve is slightly different from subsequent cycles, revealing periodic activation of electrode material (Fig. 13h). In later scans, two couples of redox peak at 1.16/1.54 and 1.36/1.6 V indicate co-intercalation/ of Zn^{2+}/Mg^{2+} into the $MgMn_2O_4$ electrode. As seen from in-situ XRD patterns (Fig. 13i), the (101) plane gradually shifts to higher 2θ angle in charging process, demonstrating the crystal framework contraction as a result of electrochemical extraction of Mg^{2+} from the tetrahedral site. When this electrode reaches 0.5 V (scan 150), the shifted peaks return to its original position. While the specific power is 70 W kg^{-1}, specific energy is 370 Wh kg^{-1}. The stable and high electrochemical performances at high currents make this emerging battery a strong competitor for exploring safe and green energy storage systems.

5. Conclusion and perspectives

ZIBs present promising potential as multivalent rechargeable aqueous ion batteries, and have received increasing research and applications. It has advantages of environmental friendliness, high capacity, high security and low cost. The commonly used negative electrode is metallic zinc. And the main factor affecting battery performance is the type of positive electrode material. This article reviews the energy storage mechanism of the vanadium-based and manganese-based cathode materials for aqueous ZIBs. It focuses on discussing the classification and important up-to-date developments of these two materials in recent years. The effective optimization methods of some electrode materials are also mentioned, such as the insertion of metal ions, selection of conductive additives, and adjustment of structural water. Tables 1 and 2 summarize the electrochemical performances of ZIBs based on various vanadium- and manganese-based cathodes and different electrolytes. The last decade has witnessed considerable progress in the field of zinc ion battery technology. However, some problems still exist and need to be resolved. The remaining challenges and perspectives for the vanadium-based and manganese-based cathode in ZIBs are hereby highlighted:

(1). Researches are constantly striving to explore various cathode materials. And there are still many critical electrochemical mechanisms and details to be clarified. The electrochemical reaction mechanisms of manganese-based electrodes can be discussed, including Zn^{2+} intercalation, conversion reaction mechanism and Zn^{2+}/H^+ co-intercalation. In addition, the valence state change of manganese during cation intercalation process and corresponding representative voltage platform still needs to be studied seriously, which may better reveal its electrochemi-

Table 1
Summary of electrochemical performances of various representative vanadium-based cathode materials for aqueous ZIBs in recent years.

Cathode material	Electrolyte	Voltage	Rate discharge capacity	Cycling performance	Reference
V_2O_5 yolk-shell microsphere	3 M $Zn(CF_3SO_3)_2$	0.4–1.4 V	410 mAh g^{-1} at 0.1 A g^{-1}, 182 mAh g^{-1} at 20 A g^{-1}	80% retained after 1000 cycles at 5 A g^{-1}	[77]
$V_2O_5{\cdot}nH_2O$	3 M $Zn(CF_3SO_3)_2$	0.2–1.6 V	372 mAh g^{-1} at 0.3 A g^{-1}, 248 mAh g^{-1} at 30 A g^{-1}	71% retained after 900 cycles at 5 A g^{-1}	[58]
spaced V_2O_5 nanosheet by acetylene black	3 M $Zn(CF_3SO_3)_2$	0.3–1.6 V	452 mAh g^{-1} at 0.1 A g^{-1}, 268 mAh g^{-1} at 30 A g^{-1}	92% retained after 5000 cycles at 10 A g^{-1}	[81]
V_2O_5 nanofibre/MWCNT	2 M $ZnSO_4$	0.2–1.6 V	375 mAh g^{-1} at 0.5 A g^{-1}, 219 mAh g^{-1} at 10 A g^{-1}	98.2% retained after 100 cycles at 1 A g^{-1}	[23]
hollow V_2O_5 nanospheres	3 M $ZnSO_4$	0.2–1.5 V	327 mAh g^{-1} at 0.1 A g^{-1}, 146 mAh g^{-1} at 20 A g^{-1}	71.3% retained after 10,000 cycles at 15 A g^{-1}	[185]
V_2O_5/PANI	3 M $Zn(CF_3SO_3)_2$	0.2–1.5 V	353.6 mAh g^{-1} at 0.1 A g^{-1}	87.5% retained after 100 cycles at 0.2 A g^{-1}	[186]
VO_2(D) hollow nanospheres	3 M $ZnSO_4$	0.2–1.5 V	448 mAh g^{-1} at 0.1 A g^{-1}, 200 mAh g^{-1} at 20 A g^{-1}	78% retained after 1200 cycles at 3 A g^{-1}	[84]
VO_2 nanorods	3 M $Zn(CF_3SO_3)_2$	0.2–1.5 V	332 mAh g^{-1} at 0.62C, 255 mAh g^{-1} at 92.9C,	99% retained after 2000 cycles at 6.2C	[86]
VO_2/rGO	3 M $Zn(CF_3SO_3)_2$	0.3–1.3 V	276 mAh g^{-1} at 0.1 A g^{-1}, 120 mAh g^{-1} at 35 A g^{-1}	99% retained after 1000 cycles at 4 A g^{-1}	[85]
V_2O_3	2 M $Zn(CF_3SO_3)_2$	0.2–1.6 V	625 mAh g^{-1} at 0.1A g^{-1}, 486 mAh g^{-1} at 20 A g^{-1}	100% retained after 10,000 cycles at 10 A g^{-1}	[90]
V_2O_3@C	3 M $Zn(CF_3SO_3)_2$	0.3–1.5 V	250 mAh g^{-1} at 2 A g^{-1}	90% retained after 4000 cycles at 5 A g^{-1}	[89]
$Li_xV_2O_5{\cdot}nH_2O$	2 M $ZnSO_4$	0.4–1.4 V	386 mAh g^{-1} at 1A g^{-1}, 170 mAh g^{-1} at 10 A g^{-1}	76.3% retained after 500 cycles at 5 A g^{-1}	[96]
$K_{0.23}V_2O_5$	2 M $Zn(CF_3SO_3)_2$	0.1–1.7 V	188 mAh g^{-1} at 0.5 A g^{-1}	92.8% retained after 500 cycles at 2 A g^{-1}	[187]
$Ca_{0.23}V_2O_5{\cdot}0.95H_2O$ nanobelt	3 M $Zn(CF_3SO_3)_2$	0.2–1.6 V	240.8 mAh g^{-1} at 5 A g^{-1}	97.7% retained after 2000 cycles at 5 A g^{-1}	[188]
$Zn_{0.25}V_2O_5{\cdot}nH_2O$ nanobelts	1 M $ZnSO_4$	0.4–1.4 V	220 mAh g^{-1} at 4.5 A g^{-1}	80% retained after 1000 cycles at 2.4 A g^{-1}	[39]
$Cu_xV_2O_5$	2 M $ZnSO_4$	0.3–1.4 V	300 mAh g^{-1} at 2 A g^{-1}	88% retained after 10,000 cycles at 10 A g^{-1}	[11]
$Ag_{0.333}V_2O_5$@$V_2O_5{\cdot}nH_2O$ coaxial nanocables	3 M $Zn(CF_3SO_3)_2$	0.2–1.8 V	245.9 mAh g^{-1} at 3 A g^{-1}	90.1% retained after 100 cycles at 0.5 A g^{-1}	[101]
LiV_3O_8	1 M $ZnSO_4$	0.6–1.2 V	230 mAh g^{-1} at 0.33 A g^{-1}, 79 mAh g^{-1} at 0.533 A g^{-1}	99% retained after 65 cycles at 0.133 A g^{-1}	[103]
$Na_2V_6O_{16}{\cdot}1.63H_2O$ nanowire	$Zn(CF_3SO_3)_2$	0.2–1.6 V	352 mAh g^{-1} at 0.05 A g^{-1}	90% retained after 6000 cycles at 5 A g^{-1}	[104]
$Na_{1.1}V_3O_{7.9}$@rGO	1 M $Zn(CF_3SO_3)_2$	0.4–1.4 V	220 mAh g^{-1} at 0.3 A g^{-1}	92.5% retained after 500 cycles at 1 A g^{-1}	[105]
$H_2V_3O_8$ nanowire/graphene	3 M $Zn(CF_3SO_3)_2$	0.2–1.6 V	394 mAh g^{-1} at 0.33C, 270 mAh g^{-1} at 20C	87% retained after 2000 cycles at 20C	[111]
$H_2V_3O_8$ nanowire/Mxene	3 M $Zn(CF_3SO_3)_2$	0.2–1.6 V	365 mAh g^{-1} at 0.2 A g^{-1}	84% retained over 5600 cycles at 5 A g^{-1}	[189]
$Na_3V_2(PO_4)_3$	0.5 M CH_3COONa/Zn $(CH_3COO)_2$	0.8–1.7 V	92 mAh g^{-1} at 0.05 A g^{-1}	77% retained over 200 cycles at 0.05 A g^{-1}	[118]
$Na_3V_2(PO_4)_3$/rGO microspheres	2 M $Zn(CF_3SO_3)_2$	0.6–1.8 V	107 mAh g^{-1} at 0.05 A g^{-1}, 88 mAh g^{-1} at 1 A g^{-1}	75% retained over 200 cycles at 0.5 A g^{-1}	[117]
$Li_3V_2(PO_4)_3$	1 M Li_2SO_4 + 2 M $ZnSO_4$	0.7–2.1 V	118 mAh g^{-1} at 0.2C	85.4% retained after 200 cycles at 0.2C	[115]
VS_2 nanosheets	1 M $ZnSO_4$	0.4–1.0 V	190.3 mAh g^{-1} at 0.05 A g^{-1}, 136.8 mAh g^{-1} at 0.5 A g^{-1}	98% retained after 200 cycles at 0.5 A g^{-1}	[125]
VS_2 nanosheets/rGO	3 M $Zn(CF_3SO_3)_2$	0.2–1.8 V	238 mAh g^{-1} at 0.1 A g^{-1}, 170 mAh g^{-1} at 5 A g^{-1}	93% retained after 1000 cycles at 5 A g^{-1}	[126]
VS_4@rGO	1 M $Zn(CF_3SO_3)_2$	0.4–1.8 V	215 mAh g^{-1} at 1 A g^{-1}	93.3% retained after 165 cycles at 1 A g^{-1}	[128]
bulk VSe_2	2 M $ZnSO_4$	0–1.6 V	250.6 mAh g^{-1} at 0.2 A g^{-1}	83% retained after 800 cycles at 2 A g^{-1}	[129]
VSe_2 nanosheets	2 M $ZnSO_4$	0.2–1.6 V	131.8 mAh g^{-1} at 0.1 A g^{-1}	80.8% retained after 500 cycles at 0.1 A g^{-1}	[130]
VN_xO_y	2 M $ZnSO_4$	0.4–1.4 V	200 mAh g^{-1} at 30 A g^{-1}	95% retained after 50 cycles at 1 A g^{-1}	[131]
V_2O_x@V_2CT_x	1 M $ZnSO_4$	0.2–1.6 V	224 mAh g^{-1} at 0.1 A g^{-1}, 107 mAh g^{-1} at 1 A g^{-1}	81.6% retained after 200 cycles at 1 A g^{-1}	[132]
V_3O_7/V_2O_5	2.5 M $Zn(CF_3SO_3)_2$		176 mAh g^{-1} at 5 A g^{-1}	96.2% retained after 1120 cycles at 2 A g^{-1}	[135]
CaV_3O_{7-x} nanobelts	1 M $ZnSO_4$	0.2–1.6 V	471.04 mAh g^{-1} at 0.83 A g^{-1}	82% retained after 400 cycles at 3.7 A g^{-1}	[136]
$(NH_4)_2V_{10}O_{25}{\cdot}8H_2O$ nanobelts	3 M $Zn(CF_3SO_3)_2$	0.3–1.3 V	366 mAh g^{-1} at 0.2 A g^{-1}, 209 mAh g^{-1} at 2 A g^{-1}	73.2% retained after 100 cycles at 0.1 A g^{-1}	[139]
$Cu_3V_2O_7(OH)_2{\cdot}2H_2O$	2.5 M $Zn(CF_3SO_3)_2$	0.2–1.6 V	216 mAh g^{-1} at 0.1 A g^{-1}	89.3% retained after 500 cycles at 0.5 A g^{-1}	[133]
V_6O_{13} nanobelts	3 M $ZnSO_4$	0.2–1.4 V	290 mAh g^{-1} at 0.375 A g^{-1}, 154 mAh g^{-1} at 18 A g^{-1}	99% retained after 1000 cycles at 9 A g^{-1}	[190]
$V_{1-x}Al_xO_{1.52}(OH)_{0.77}$	1 M $ZnSO_4$	0.2–1.13 V	68 mAh g^{-1} at 0.6 A g^{-1}	80% retained after 50 cycles at 0.015 A g^{-1}	[140]

Table 2
Summary of electrochemical performances of various representative manganese-based cathode materials for aqueous ZIBs in recent years.

Cathode material	Electrolyte	Voltage	Rate discharge capacity	Cycling performance	Reference
MnO/C@rGO	2 M $ZnSO_4$	0.8–1.9 V	314.9 mAh g^{-1} at 0.1 A g^{-1}, 110.1 mAh g^{-1} at 2 A g^{-1}	99% retained after 300 cycles at 0.5 A g^{-1}	[191]
carbon-coated MnO nanoparticle	2 M $ZnSO_4$ + 0.1 M $MnSO_4$	0.8–1.8 V	300 mAh g^{-1} at 0.1 A g^{-1}, 105 mAh g^{-1} at 2 A g^{-1}	99.3% retained after 1500 cycles at 1 A g^{-1}	[192]
δ-MnO_2 submicrospheres	1 M $ZnSO_4$ + 0.1 M $MnSO_4$	1–1.8 V	133 mAh g^{-1} at 0.2 A g^{-1}	91% retained after 100 cycles at 0.1 A g^{-1}	[150]
β-MnO_2@C	3 M $Zn(CF_3SO_3)_2$ + 0.1 M $MnSO_4$	1–1.8 V	121 mAh g^{-1} at 0.1 A g^{-1}, 50 mAh g^{-1} at 2 A g^{-1}	98% retained after 230 cycles at 0.3 A g^{-1}	[155]
yolk-shell MnO_2@C nanowires	$ZnSO_4$ + $MnSO_4$	0.8–1.8 V	239 mAh g^{-1} at 0.1 A g^{-1}, 91 mAh g^{-1} at 2 A g^{-1}	99% retained after 1000 cycles at 1 A g^{-1}	[147]
NHCSs@MnO_2	2 M $ZnSO_4$ + 0.1 M $MnSO_4$	0.8–1.8 V	206 mAh g^{-1} at 0.1 A g^{-1}, 103 mAh g^{-1} at 0.5 A g^{-1}	98.3% retained after 650 cycles at 0.5 A g^{-1}	[156]
α-MnO_2/CNT	2 M $ZnSO_4$ + 0.1 M $MnSO_4$	1–1.85 V	296 mAh g^{-1} at 0.2 A g^{-1}, 80 mAh g^{-1} at 3 A g^{-1}	96% retained after 10,000 cycles at 3 A g^{-1}	[158]
α-MnO_2/graphene scrolls	2 M $ZnSO_4$ + 0.2 M $MnSO_4$	1–1.8 V	282 mAh g^{-1} at 0.3 A g^{-1}, 165.7 mAh g^{-1} at 3 A g^{-1}	94% retained after 3000 cycles at 3 A g^{-1}	[159]
α-MnO_2@PPy nanorods	2 M $ZnSO_4$ + 0.1 M $MnSO_4$	1–1.8 V	114 mAh g^{-1} at 0.4 A g^{-1}	65% retained after 100 cycles at 0.1 A g^{-1}	[193]
Na^+-intercalated δ-MnO_2 nanoflakes	2 M $ZnSO_4$ + 0.2 M $MnSO_4$	0.9–1.8 V	281 mAh g^{-1} at 1 A g^{-1}, 131 mAh g^{-1} at 6 A g^{-1}	93% retained after 1000 cycles at 4 A g^{-1}	[163]
α-$K_{0.19}MnO_2$ nanotubes	3 M $Zn(CF_3SO_3)_2$ + 0.2 M Mn $(CF_3SO_3)_2$	0.8–1.9 V	113 mAh g^{-1} at 20C	76% retained after 200 cycles at 2C	[164]
$Ca_{0.28}MnO_2{\cdot}0.5H_2O$	1 M $ZnSO_4$ + 0.1 M $MnSO_4$	0.4–1.9 V	295 mAh g^{-1} at 0.175 A g^{-1}, 124 mAh g^{-1} at 3.5 A g^{-1}	95% retained after 5000 cycles at 3.5 A g^{-1}	[61]
La-Ca co-doped ε-MnO_2	1 M $ZnSO_4$ + 0.4 M $MnSO_4$	0.8–1.9 V	294 mAh g^{-1} at 0.2 A g^{-1}, 161 mAh g^{-1} at 1.6 A g^{-1}	76.8% retained after 200 cycles at 0.2 A g^{-1}	[162]
Mesoporous MnO_2 flower stabilized by Zn^{2+}	2 M $ZnSO_4$ + 0.1 M $MnSO_4$	1–1.9 V	275 mAh g^{-1} at 0.3 A g^{-1}, 124 mAh g^{-1} at 3 A g^{-1}	75% retained after 2000 cycles at 3 A g^{-1}	[161]
α-Mn_2O_3	2 M $ZnSO_4$	1–1.9 V	137 mAh g^{-1} at 0.1 A g^{-1}, 57 mAh g^{-1} at 1 A g^{-1}	87% retained after 30 cycles at 0.1 A g^{-1}	[166]
Mesoporous Mn_2O_3	2 M $ZnSO_4$ + 0.2 M $MnSO_4$	1–1.8 V	292 mAh g^{-1} at 0.616 A g^{-1}, 162 mAh g^{-1} at 3.08 A g^{-1}	89% retained after 3000 cycles at 3.08 A g^{-1}	[169]
α-MnO_2/Mn_2O_3	2 M $ZnSO_4$ + 0.2 M $MnSO_4$	1–1.9 V	322.1 mAh g^{-1} at 0.2 A g^{-1}, 213.6 mAh g^{-1} at 3 A g^{-1}	86.2% retained after 1000 cycles at 3 A g^{-1}	[194]
MOF-derived α-Mn_2O_3	2 M $ZnSO_4$ + 0.2 M $MnSO_4$	1–1.85 V	225 mAh g^{-1} at 0.05 A g^{-1}, 140 mAh g^{-1} at 0.5 A g^{-1}	70% retained after 1600 cycles at 2 A g^{-1}	[45]
Mn_2O_3/Al_2O_3	2 M $ZnSO_4$ + 0.1 M $MnSO_4$	1–1.8 V	118 mAh g^{-1} at 1.5 A g^{-1}	98% retained after 1100 cycles at 1.5 A g^{-1}	[170]
Mn_3O_4 nanoflower	2 M $ZnSO_4$ + 0.1 M $MnSO_4$	1–1.8 V	296 mAh g^{-1} at 0.1 A g^{-1}, 125 mAh g^{-1} at 0.5 A g^{-1}	99.5% retained after 500 cycles at 0.5 A g^{-1}	[173]
Porous cube-like Mn_3O_4@C	2 M $ZnSO_4$ + 0.1 M $MnSO_4$	0.8–1.9 V	323.2 mAh g^{-1} at 0.1 A g^{-1}, 102.3 mAh g^{-1} at 2 A g^{-1}	77.1% retained after 200 cycles at 0.5 A g^{-1}	[177]
α-Mn_3O_4@C	2 M $ZnSO_4$ + 0.1 M $MnSO_4$	0.8–1.9 V	300 mAh g^{-1} at 0.1 A g^{-1}, 80 mAh g^{-1} at 0.8 A g^{-1}	100% retained after 1000 cycles at 0.6 A g^{-1}	[178]
Mn_3O_4@NC nanorods	2 M $ZnSO_4$ + 0.1 M $MnSO_4$	0.9–1.8 V	280 mAh g^{-1} at 0.1 A g^{-1}	100% retained after 700 cycles at 1 A g^{-1}	[179]
$LiMn_2O_4$/GN/CNT	0.5 M $Zn(CH_3COO)_2$ + 0.5 M $LiCH_3COO$	1.2–2.2 V	130 mAh g^{-1} at 0.2C, 100 mAh g^{-1} at 5C	82.1% retained after 600 cycles at 2C	[180]
$ZnMn_2O_4$/C	3 M $Zn(CF_3SO_3)_2$	0.8–2.0 V	72 mAh g^{-1} at 2 A g^{-1}	94% retained after 500 cycles at 0.5 A g^{-1}	[183]
$MgMn_2O_4$	1 M $MgSO_4$ + $ZnSO_4$ + 0.1 M $MnSO_4$	0.5–1.9 V	247 mAh g^{-1} at 0.1 A g^{-1}, 76 mAh g^{-1} at 1.2 A g^{-1}	80% retained after 500 cycles at 0.5 A g^{-1}	[184]

cal mechanism, thus providing effective guidance for the construction of manganese-based electrode ZIBs with high energy density and enhanced performance. The use of advanced characterization techniques and a variety of electrochemical methods as well as the development of accurate theoretical calculations is an urgent need to solve this challenge.

(2). Manganese-based cathode materials may continuously dissolve in the electrolyte solution. Therefore, it is necessary to formulate a useful and novel strategy to prevent the dissolution of manganese, such as adding additives in the electrolyte, adjusting pH of electrolyte, or growing a protective layer on the surface of the manganese-based cathode. In aqueous solution, capacity decline of MnO_2 is mainly because of the dissolution of active material and structural transformation caused by the disproportionation reaction of Mn^{3+}. Adding Mn^{2+} salt in the electrolyte in advance can suppress this side reaction. The addition of Mn^{2+} changes the balance between the dissolution and reoxidation of Mn^{2+}. It is conducive to forming a uniform amorphous MnO protective layer on the surface of cathode electrode, to maintain the integrity of the electrode.

(3). The vanadium-based compound has a large interlayer distance that can accommodate rapid insertion/extraction of Zn^{2+}, and generally has a higher specific capacity and rate performance than the manganese-based compound. However, with multiple charge and discharge reactions, the layer structure is gradually damaged. Inserting metal ions between layers as pillars is an effective way to enhance the stability of the layered structure. On the other hand, the type/quantity of pre-inserted metal ions may inhibit the intercalation of zinc ions and may cause the phase change. Therefore, it is necessary to further understand the influence of pre-inserted metal ions on the crystal structure of the host material, and construct the structure–activity relationship between the type/quantity of metal ions and

the electrochemical performance. Ensure that the layered structure is strengthened through multiple insertion/extraction of Zn^{2+}.

(4). The specific capacity of the reported cathode material is far from matching the high capacity of zinc anode (820 mAh g^{-1}). This mismatch requires researches on new cathode materials with a novel zinc storage mechanism to increase the capacity, such as simultaneous cation and anion redox reactions. Reversible anionic redox, such as N^{3-}/N^{2-}, contributes to fast reaction dynamics and high reversible capacity. In-depth discussion and researches on the reaction mechanism during the cycling process are required. In-situ characterizations, including in-situ TEM, Raman, XRD are suggested.

(5). The divalent Zn^{2+} has a strong electrostatic interaction with the cathode electrode skeleton, resulting in the slow diffusion of Zn^{2+}. To improve zinc storage performance, pre-intercalation of ions and water, bulk doping, increase of interplanar spacing, defect chemistry and nanostructure engineering can be used. Vanadium-based oxides containing interlayer cations or structural water usually have an expanded layered structure, which facilitates the insertion of hydrated Zn^{2+}. Dissolved water acts as a charge shield to buffer the high charge density of divalent Zn^{2+} and promote the transport of Zn^{2+}. It is worth noting that V^{4+}/V^{5+} mixed-valence compounds are not only beneficial for electrochemically adapting to the storage of large amounts of Zn^{2+}, but also conducive to the smooth evolution of the vanadium valence state.

(6). Many cathode materials have low conductivity, limiting rate performance of batteries. Based on these issues, strategies for compositing with conductive carbon-based materials (such as carbon nanotubes, graphene, acetylene black and carbon black), surface coating, electrolyte optimization, and combination with conductive polymers (such as PANI and PEDOT) could improve electrode conductivity and performance. Except for inorganic cathode hosts, organic cathode materials with rich precursors and flexible structures may also become attractive candidates for non-aqueous and aqueous battery systems in the future.

In summary, the development of aqueous ZIBs requires further systematic and scientific researches to meet large-scale practical needs. It is of great significance to continuously explore and optimize innovative cathode materials, stable anode materials and cheap electrolytes. The environment-friendly and high energy density aqueous ZIBs have broad development and application prospects in the future.

Declaration of Competing Interest

The authors declare that they have no known competing financial interests or personal relationships that could have appeared to influence the work reported in this paper.

Acknowledgements

This work was financially supported by the National Natural Science Foundation of China (No. 51872090, 51772097), the Hebei Natural Science Fund for Distinguished Young Scholar (No. E2019209433, E2017209079). H Wang thanks for the financial support from Hunan Provincial Science and Technology Plan Project of China (No. 2016TP1007, 2017TP1001, and 2018RS3009).

References

[1] K.H. Dunn B, J.M. Tarascon, Science 334 (2011) 928–935.
[2] C.C. Li, Q.X. Liu, J. Energy Storage 29 (2020) 101339–101348.
[3] C. Li, B. Zhang, B. Xie, X. Zhao, J. Chen, Energy Convers. Manage. 208 (2020) 112586–112598.
[4] D. Cheng, Y. Li, J. Zhang, M. Tian, B. Wang, Z. He, L. Dai, L. Wang, Carbon 170 (2020) 527–542.
[5] B. Hu, L. Li, X. Xiong, L. Liu, C. Huang, D. Yu, C. Chen, J. Solid State Electrochem. 23 (2019) 1315–1324.
[6] X.T. Gao, X.D. Zhu, L.L. Gu, C. Wang, K.N. Sun, Y.L. Hou, Chem. Eng. J. 378 (2019) 122189–122197.
[7] H. Fan, C. Gao, H. Jiang, Q. Dong, B. Hong, Y. Lai, J. Energy Chem. 49 (2020) 59–70.
[8] Z. Jiang, C. Han, Z.Q. Huang, X.W. Wu, Z.X. He, W. Meng, L. Dai, L. Wang, J. Electrochem. Soc. 167 (2020) 20550–20556.
[9] D.J. Kim, R. Ponraj, A.G. Kannan, H.-W. Lee, R. Fathi, R. Ruffo, C.M. Mari, D.K. Kim, J. Power Sources 244 (2013) 758–763.
[10] Q. Zheng, H. Yi, X. Li, H. Zhang, J. Energy Chem. 27 (2018) 1597–1617.
[11] Y. Yang, Y. Tang, S. Liang, Z. Wu, G. Fang, X. Cao, C. Wang, T. Lin, A. Pan, J. Zhou, Nano Energy 61 (2019) 617–625.
[12] C. Li, X. Shi, S. Liang, X. Ma, M. Han, X. Wu, J. Zhou, Chem. Eng. J. 379 (2020) 122248–122256.
[13] S. Lu, M. Wang, F. Guo, J. Tu, A. Lv, Y. Chen, S. Jiao, Chem. Eng. J. 389 (2020) 124370–1123479.
[14] H.Y. Xu, H.W. Lai, Z. Li, X.Z. Dong, S.Y. Cai, X.Y. Chu, C. Gao, J. Energy Chem. 45 (2020) 40–44.
[15] J. Xia, K. Jiang, J. Xie, S. Guo, L. Liu, Y. Zhang, S. Nie, Y. Yuan, H. Yan, X. Wang, Chem. Eng. J. 359 (2019) 1244–1251.
[16] P. Vishnuprakash, C. Nithya, M. Premalatha, Electrochim. Acta 309 (2019) 234–241.
[17] Z. Jiang, Y. Li, C. Han, Z. He, W. Ma, W. Meng, Y. Jiang, L. Dai, L. Wang, Ceram. Int. 46 (2020) 1954–1961.
[18] A. Ponrouch, C. Frontera, F. Bardé, M.R. Palacín, Nat. Mater. 15 (2015) 169–172.
[19] E. Zhang, B. Wang, J. Wang, H. Ding, S. Zhang, H. Duan, X. Yu, B. Lu, Chem. Eng. J. 389 (2020) 124407–124414.
[20] G.A. Elia, K. Marquardt, K. Hoeppner, S. Fantini, R. Lin, E. Knipping, W. Peters, J.-F. Drillet, S. Passerini, R. Hahn, Adv. Mater. 28 (2016) 7564–7579.
[21] H. Zhang, K. Ye, K. Zhu, R. Cang, J. Yan, K. Cheng, G. Wang, D. Cao, Chem-Eur. J. 23 (2017) 17118–17126.
[22] X. Sun, L. Blanc, G.M. Nolis, P. Bonnick, J. Cabana, L.F. Nazar, Chem. Mater. 30 (2017) 121–128.
[23] Y. Li, Z. Huang, P.K. Kalambate, Y. Zhong, Z. Huang, M. Xie, Y. Shen, Y. Huang, Nano Energy 60 (2019) 752–759.
[24] B. Tang, L. Shan, S. Liang, J. Zhou, Energy Environ. Sci. 12 (2019) 3288–3304.
[25] S. Islam, V. Mathew, J.J. Song, S.J. Kim, S. Kim, J.P. Baboo, D.T. Pham, D.Y. Putro, Y.K. Sun, J. Kim, J. Mater. Chem. A 5 (2017) 23299–23309.
[26] G. Fang, J. Zhou, A. Pan, S. Liang, ACS Energy Lett. 3 (2018) 2480–2501.
[27] C. Xu, B. Li, H. Du, F. Kang, Angew. Chem. 51 (2012) 933–935.
[28] M. Song, H. Tan, D. Chao, H.J. Fan, Adv. Funct. Mater. 28 (2018) 1802564–1802590.
[29] P. Gu, M. Zheng, Q. Zhao, X. Xiao, H. Xue, H. Pang, J. Mater. Chem. A 5 (2017) 7651–7666.
[30] W. Zhou, J. Chen, M. Chen, X. Xu, Q. Tian, J. Xu, C.-P. Wong, RSC Adv. 9 (2019) 30556–30564.
[31] X. Zeng, J. Hao, Z. Wang, J. Mao, Z. Guo, Energy Storage Mater. 20 (2019) 410–437.
[32] W. Xu, Y. Wang, Nano-Micro Lett. 11 (2019) 90–119.
[33] M.H. Alfaruqi, S.J. Kim, J. Song, J. Jo, S. Kim, V. Mathew, J. Kim, J. Power Sources 288 (2015) 320–327.
[34] F.R. McLarnon, J. Electrochem. Soc. 138 (1991) 645–664.
[35] J. Zhou, Z.X. Wu, X. Guo, G.Z. Fang, S.Q. Liang, Chem. Commun. 54 (2018) 4457–4460.
[36] L. Chen, Q. An, L. Mai, Adv. Mater. Interfaces 6 (2019) 1900387–1900410.
[37] J. Ding, Z. Du, L. Gu, B. Li, L. Wang, S. Wang, Y. Gong, S. Yang, Adv. Mater. 30 (2018) 1800762–1800767.
[38] C. Li, X. Zhang, W. He, G. Xu, R. Sun, J. Power Sources 449 (2020) 227596–227613.
[39] D. Kundu, B.D. Adams, V. Duffort, S.H. Vajargah, L.F. Nazar, Nat. Energy 1 (2016) 16119–16126.
[40] K. Wu, J. Huang, J. Yi, X. Liu, Y. Liu, Y. Wang, J. Zhang, Y. Xia, Adv. Energy Mater. 10 (2020) 1903977–1904008.
[41] X. Chen, L. Wang, H. Li, F. Cheng, J. Chen, J. Energy Chem. 38 (2019) 20–25.
[42] Y. Zhang, A. Chen, J. Sun, J. Energy Chem. 54 (2021) 655–667.
[43] X.M. Xu, F.Y. Xiong, J.S. Meng, X.P. Wang, C.J. Niu, Q.Y. An, L.Q. Mai, Adv. Funct. Mater. 30 (2020) 1904398–1904433.
[44] N. Zhang, X. Chen, M. Yu, Z. Niu, F. Cheng, J. Chen, Chem. Soc. Rev. 49 (2020) 4203–4219.
[45] M. Mao, X. Wu, Y. Hu, Q. Yuan, Y.-B. He, F. Kang, J. Energy Chem. 52 (2021) 277–283.
[46] C. Yuan, Y. Zhang, Y. Pan, X. Liu, G. Wang, D. Cao, Electrochim. Acta 116 (2014) 404–412.
[47] N. Zhang, F.Y. Cheng, J.X. Liu, L.B. Wang, X.H. Long, X.S. Liu, F.J. Li, J. Chen, Nat. Commun. 8 (2017) 405–413.

[48] J.S. Park, J.H. Jo, Y. Aniskevich, A. Bakavets, G. Ragoisha, E. Streltsov, J. Kim, S.T. Myung, Chem. Mater. 30 (2018) 6777–6787.
[49] L.E. Blanc, D. Kundu, L.F. Nazar, Joule 4 (2020) 771–799.
[50] D. Chen, M. Lu, D. Cai, H. Yang, W. Han, J. Energy Chem. 54 (2021) 712–726.
[51] D. Bin, W. Huo, Y. Yuan, J. Huang, Y. Liu, Y. Zhang, F. Dong, Y. Wang, Y. Xia, Chem 6 (2020) 968–984.
[52] P. Gao, Q. Ru, H.L. Yan, S.K. Cheng, Y. Liu, X.H. Hou, L. Wei, F.C.C. Ling, ChemElectroChem 7 (2020) 283–288.
[53] W. Sun, F. Wang, S. Hou, C. Yang, X. Fan, Z. Ma, T. Gao, F. Han, R. Hu, M. Zhu, C. Wang, J. Am. Chem. Soc. 139 (2017) 9775–9778.
[54] X. Gao, H.W. Wu, W.J. Li, Y. Tian, Y. Zhang, H. Wu, L. Yang, G.Q. Zou, H.S. Hou, X.B. Ji, Small 16 (2020) 1905842–1905851.
[55] F. Wan, L.L. Zhang, X. Dai, X.Y. Wang, Z.Q. Niu, J. Chen, Nat. Commun. 9 (2018) 1656–1666.
[56] N. Zhang, Y. Dong, M. Jia, X. Bian, Y.Y. Wang, M.D. Qiu, J.Z. Xu, Y.C. Liu, L.F. Jiao, F.Y. Cheng, ACS Energy Lett. 3 (2018) 1366–1372.
[57] H. Ren, J. Zhao, L. Yang, Q.H. Liang, S. Madhavi, Q.Y. Yan, Nano Res. 12 (2019) 1347–1353.
[58] M. Yan, P. He, Y. Chen, S. Wang, Q. Wei, K. Zhao, X. Xu, Q. An, Y. Shuang, Y. Shao, K.T. Mueller, L. Mai, J. Liu, J. Yang, Adv. Mater. 30 (2018) 1703725–1703730.
[59] J.W. Lai, H.H. Zhu, X.P. Zhu, H. Koritala, Y. Wang, ACS Appl. Energy Mater. 2 (2019) 1988–1996.
[60] K.Y. Zhu, T. Wu, K. Huang, Adv. Energy Mater. 9 (2019) (1979) 1901968–1902190.
[61] T.J. Sun, Q.S. Nian, S.B. Zheng, J.Q. Shi, Z.L. Tao, Small 16 (2020) 2000597–2000604.
[62] X.Z. Zhai, J. Qu, S.M. Hao, Y.Q. Jing, W. Chang, J. Wang, W. Li, Y. Abdelkrim, H.F. Yuan, Z.Z. Yu, Nano-Micro Lett. 12 (2020) 56–70.
[63] H.L. Pan, Y.Y. Shao, P.F. Yan, Y.W. Cheng, K.S. Han, Z.M. Nie, C.M. Wang, J.H. Yang, X.L. Li, P. Bhattacharya, K.T. Mueller, J. Liu, Nat. Energy 1 (2016) 16039–16045.
[64] D.L. Chao, W.H. Zhou, C. Ye, Q.H. Zhang, Y.G. Chen, L. Gu, K. Davey, S.Z. Qiao, Angew. Chem. Int. Ed. 58 (2019) 7823–7828.
[65] Y. Jin, L. Zou, L. Liu, M.H. Engelhard, R.L. Patel, Z. Nie, K.S. Han, Y. Shao, C. Wang, J. Zhu, H. Pan, J. Liu, Adv. Mater. 31 (2019) 1900567–1900574.
[66] W. Liu, X. Zhang, Y. Huang, B. Jiang, Z. Chang, C. Xu, F. Kang, J. Energy Chem. 56 (2021) 365–373.
[67] V. Soundharrajan, B. Sambandam, S. Kim, S. Islam, J. Jo, S. Kim, V. Mathew, Y.K. Sun, J. Kim, Energy Storage Mater. 28 (2020) 407–417.
[68] X. Guo, J. Zhou, C. Bai, X. Li, G. Fang, S. Liang, Mater. Today Energy 16 (2020) 100396–100403.
[69] B. Lee, H.R. Seo, H.R. Lee, C.S. Yoon, J.H. Kim, K.Y. Chung, B.W. Cho, S.H. Oh, ChemSusChem 9 (2016) 2948–2956.
[70] P. Chen, G. Zheng, G. Guo, Z. Wang, J. Tang, S. Li, Z. Wen, S. Ji, J. Sun, J. Alloys Compd. 784 (2019) 574–583.
[71] J. Yao, Y. Li, R.C. Massé, E. Uchaker, G. Cao, Energy Storage Mater. 11 (2018) 205–259.
[72] C. Niu, X. Liu, J. Meng, L. Xu, M. Yan, X. Wang, G. Zhang, Z. Liu, X. Xu, L. Mai, Nano Energy 27 (2016) 147–156.
[73] F. Wan, Z. Niu, Angew. Chem. Int. Ed. 58 (2019) 16358–16367.
[74] S. Wang, T. Yu, Y. Li, H. Fu, C. Sun, Mater. Res. Bull. 111 (2019) 284–288.
[75] H. Yu, X. Rui, H. Tan, J. Chen, X. Huang, C. Xu, W. Liu, D.Y.W. Yu, H.H. Hng, H.E. Hoster, Q. Yan, Nanoscale 5 (2013) 4937–4943.
[76] H. Qin, L. Chen, L. Wang, X. Chen, Z. Yang, Electrochim. Acta 306 (2019) 307–316.
[77] R. Li, Q. Zheng, X.F. Li, J. Mater. Chem. A 8 (2020) 5186–5193.
[78] F. Liu, Z. Chen, G. Fang, Z. Wang, Y. Cai, B. Tang, J. Zhou, S. Liang, Nano-Micro Lett. 11 (2019) 25–35.
[79] Y. Chen, K. Xiang, Y. Zhu, L. Xiao, W. Chen, H. Liao, X. Chen, H. Chen, J. Electrochem. Soc. 166 (2019) A2805–A2813.
[80] P. Hu, T. Zhu, J. Ma, C. Cai, G. Hu, X. Wang, Z. Liu, L. Zhou, L. Mai, Chem. Commun. 55 (2019) 8486–8489.
[81] X.Y. Wang, J.C. Sun, ACS Appl. Mater. & Inter. 11 (2019) 41297–41303.
[82] S. Deng, Z. Yuan, Z. Tie, C. Wang, L. Song, Z. Niu, Angew. Chem. Int. Ed. (2020), https://doi.org/10.1002/anie.202010287.
[83] X.H. Rui, D.H. Sim, C. Xu, W.L. Liu, H.T. Tan, K.M. Wong, H.H. Hng, T.M. Lim, Q. Y. Yan, RSC Adv. 2 (2012) 1174–1180.
[84] L. Chen, Z. Yang, Y. Huang, Nanoscale 11 (2019) 13032–13039.
[85] X. Dai, F. Wan, L. Zhang, H. Cao, Z. Niu, Energy Storage Mater. 17 (2019) 143–150.
[86] L. Ma, X. Wang, J. Sun, J. Electroanal. Chem. 873 (2020) 114395–114400.
[87] H. Luo, B. Wang, C. Wang, F. Wu, F. Jin, B. Cong, Y. Ning, Y. Zhou, D. Wang, H. Liu, S. Dou, Energy Storage Mater. 33 (2020) 390–398.
[88] W. Gou, X. Kong, Y. Wang, Y. Ai, S. Liang, A. Pan, G. Cao, Chem. Eng. J. 374 (2019) 545–553.
[89] Y.C. Ding, Y.Q. Peng, S.H. Chen, X.X. Zhang, Z.Q. Li, L. Zhu, L.E. Mo, L.H. Hu, ACS Appl. Mater. & Inter. 11 (2019) 44109–44117.
[90] H. Luo, B. Wang, F. Wang, J. Yang, F. Wu, Y. Ning, Y. Zhou, D. Wang, H. Liu, S. Dou, ACS Nano 14 (2020) 7328–7337.
[91] C. Peng, F. Xiao, J. Yang, Z. Li, G. Lei, Q. Xiao, Y. Ding, Z. Hu, Electrochim. Acta 192 (2016) 216–226.
[92] S. Li, M. Chen, G. Fang, L. Shan, X. Cao, J. Huang, S. Liang, J. Zhou, J. Alloys Compd. 801 (2019) 82–89.
[93] P. He, G. Zhang, X. Liao, M. Yan, X. Xu, Q. An, J. Liu, L. Mai, Adv. Energy Mater. 8 (2018) 1702463–1702468.
[94] R. Baddour-Hadjean, L. Thanh Nguyen Huynh, D. Batyrbekuly, S. Bach, J.P. Pereira-Ramos, ChemSusChem 12 (2019) 5192–5198.
[95] G. Fang, C. Liang, J. Zhou, G. Cai, S. Liang, J. Liu, Electrochim. Acta 218 (2016) 199–207.
[96] Y.Q. Yang, G.Z. Fang, L.T. Shan, J.S. Guo, W.Y. Zhang, J. Zhou, C. Wang, L.B. Wang, S.Q. Liang, Energy Environ. Sci. 11 (2018) 3157–3162.
[97] S. Islam, D.Y. Putro, V. Soundharrajan, B. Sambandam, J. Jo, S. Park, S. Lee, V. Mathew, J. Kim, J. Mater. Chem. A 7 (2019) 20335–20347.
[98] C. Xia, P. Li, X.X. Zhang, H.N. Alshareef, Angew. Chem. Int. Ed. 57 (2018) 3943–3948.
[99] P. Hu, M. Yan, T. Zhu, X. Wang, X. Wei, J. Li, L. Zhou, Z. Li, L. Chen, L. Mai, ACS Appl. Mater. & Inter. 9 (2017) 42717–42722.
[100] L.T. Ma, N. Li, C.B. Long, B.B. Dong, D.L. Fang, Z.X. Liu, Y.W. Zhao, X.L. Li, J. Fan, S. M. Chen, S.J. Zhang, C.Y. Zhi, Adv. Funct. Mater. 29 (2019) 1906142–1906151.
[101] J. Zeng, W.Q. Wang, X. Wei, C.Y. Liu, H.G. Peng, Z.H. Zhang, X.S. Guo, G.C. Li, Inorg. Chem. Front. 6 (2019) 2339–2348.
[102] B. Tang, G. Fang, J. Zhou, L. Wang, Y. Lei, C. Wang, T. Lin, Y. Tang, S. Liang, Nano Energy 51 (2018) 579–587.
[103] M.H. Alfaruqi, V. Mathew, J. Song, S. Kim, S. Islam, D.T. Pham, J. Jo, S. Kim, J.P. Baboo, Z. Xiu, K.-S. Lee, Y.-K. Sun, J. Kim, Chem. Mater. 29 (2017) 1684–1694.
[104] P. Hu, T. Zhu, X. Wang, X. Wei, M. Yan, J. Li, W. Luo, W. Yang, W. Zhang, L. Zhou, Z. Zhou, L. Mai, Nano Lett. 18 (2018) 1758–1763.
[105] Y. Cai, F. Liu, Z. Luo, G. Fang, J. Zhou, A. Pan, S. Liang, Energy Storage Mater. 13 (2018) 168–174.
[106] Z.W. Liu, W. Wei, P. Jing, X. Li, Q.Y. Zhu, H.J. Sun, Y.Y. Dong, G.S. Zakharova, Solid State Ionics 329 (2019) 74–81.
[107] M.H. Rastgoo-Deylami, J.W. Hong, S. Tae, ChemistrySelect 4 (2019) 11711–11717.
[108] Z.Y. Cao, H. Zhang, Y.N. Ge, R. Clemente, P. Dong, L.P. Wang, J.F. Shen, M.X. Ye, P.M. Ajayan, J. Mater. Chem. A 7 (2019) 25262–25267.
[109] M.R. Deylami, S.T. Hong, Chem. Mater. 30 (2018) 7464–7472.
[110] P. He, Y. Quan, X. Xu, M. Yan, W. Yang, Q. An, L. He, L. Mai, Small 13 (2017) 1702551–1702557.
[111] Q. Pang, C. Sun, Y. Yu, K. Zhao, Z. Zhang, P.M. Voyles, G. Chen, Y. Wei, X. Wang, Adv. Energy Mater. 8 (2018) 1800144–1800152.
[112] Z. Jiang, Y. Li, J. Zhu, B. Li, C. Li, L. Wang, W. Meng, Z. He, L. Dai, J. Alloys Compd. 791 (2019) 176–183.
[113] H. Yan, Y. Fu, X. Wu, X. Xue, C. Li, L. Zhang, Solid State Ionics 336 (2019) 95–101.
[114] P. Wei, Y. Liu, Y. Su, L. Miao, Y. Huang, Y. Liu, Y. Qiu, Y. Li, X. Zhang, Y. Xu, X. Sun, C. Fang, Q. Li, J. Han, Y. Huang, ACS Appl. Mater. & Inter. 11 (2019) 3116–3124.
[115] H.B. Zhao, C.J. Hu, H.W. Cheng, J.H. Fang, Y.P. Xie, W.Y. Fang, T.N. Doan, T.K. Hoang, J.Q. Xu, P. Chen, Sci. Rep. 6 (2016) 25809–25818.
[116] G. Li, Z. Yang, Y. Jiang, C. Jin, W. Huang, X. Ding, Y. Huang, Nano Energy 25 (2016) 211–217.
[117] P. Hu, T. Zhu, X. Wang, X. Zhou, X. Wei, X. Yao, W. Luo, C. Shi, K.A. Owusu, L. Zhou, L. Mai, Nano Energy 58 (2019) 492–498.
[118] G. Li, Z. Yang, Y. Jiang, W. Zhang, Y. Huang, J. Power Sources 308 (2016) 52–57.
[119] C.W. Mason, F. Lange, E.C.S. Electrochem, Lett. 4 (2015) A79–A82.
[120] W. Li, K. Wang, S. Cheng, K. Jiang, Energy Storage Mater. 15 (2018) 14–21.
[121] Y.S. Wang, N.H. Song, T.J. Zhang, Q.L. Zhang, D.P. Yang, F. Wang, Chem. Phys. Lett. 741 (2020) 137121–137126.
[122] D. Wu, C. Wang, M. Wu, Y. Chao, P. He, J. Ma, J. Energy Chem. 43 (2020) 24–32.
[123] P. Jing, H. Lu, W. Yang, Y. Cao, Electrochim. Acta 330 (2020) 135263–135272.
[124] T. Jiao, Q. Yang, S. Wu, Z. Wang, D. Chen, D. Shen, B. Liu, J. Cheng, H. Li, L. Ma, C. Zhi, W. Zhang, J. Mater. Chem. A 7 (2019) 16330–16338.
[125] P. He, M. Yan, G. Zhang, R. Sun, L. Chen, Q. An, L. Mai, Adv. Energy Mater. 7 (2017) (1924) 1601920–1602160.
[126] T. Chen, X. Zhu, X. Chen, Q. Zhang, Y. Li, W. Peng, F. Zhang, X. Fan, J. Power Sources 477 (2020) 228652–228659.
[127] Q.C. Zhu, Q. Xiao, B.W. Zhang, Z.C. Yan, X. Liu, S. Chen, Z.F. Ren, Y. Yu, J. Mater. Chem. A 8 (2020) 10761–10766.
[128] H. Qin, Z. Yang, L. Chen, X. Chen, L. Wang, J. Mater. Chem. A 6 (2018) 23757–23765.
[129] L.L. Wang, Z.X. Wu, M.J.H. Jiang, J.Y. Lu, Q.H. Huang, Y. Zhang, L.J. Fu, M. Wu, Y. P. Wu, J. Mater. Chem. A 8 (2020) 9313–9321.
[130] Z. Wu, C. Lu, Y. Wang, L. Zhang, L. Jiang, W. Tian, C. Cai, Q. Gu, Z. Sun, L. Hu, Small 16 (2020) 2000698–2000707.
[131] G.Z. Fang, S.Q. Hang, Z.X. Chen, P.X. Cui, X.S. Zheng, A.Q. Pan, B.G. Lu, X.H. Lu, J. Zhou, Adv. Funct. Mater. 29 (2019) 1905267–1905275.
[132] R. Venkatkarthick, N. Rodthongkum, X. Zhang, S. Wang, P. Pattananuwat, Y. Zhao, R. Liu, J. Qin, ACS Appl. Energy Mater. 3 (2020) 4677–4689.
[133] L. Chen, Z. Yang, J. Wu, H. Chen, J. Meng, Electrochim. Acta 330 (2020) 135347–135353.
[134] B. Sambandam, V. Soundharrajan, S. Kim, M.H. Alfaruqi, J. Jo, S. Kim, V. Mathew, Y.-K. Sun, J. Kim, J. Mater. Chem. A 6 (2018) 3850–3856.
[135] H. Chen, L. Chen, J. Meng, Z. Yang, J. Wu, Y. Rong, L. Deng, Y. Shi, J. Power Sources 474 (2020) 228569–228578.
[136] X. Liang, J. Hao, B. Tan, X. Lu, W. Li, J. Power Sources 472 (2020) 228507–228513.
[137] L. Shan, J. Zhou, W. Zhang, C. Xia, S. Guo, X. Ma, G. Fang, X. Wu, S. Liang, Energy Technol. 7 (2019) 1900022–1900041.

[138] B. Tang, J. Zhou, G. Fang, S. Guo, X. Guo, L. Shan, Y. Tang, S. Liang, J. Electrochem. Soc. 166 (2019) A480–A486.
[139] H. Jiang, Y. Zhang, Z. Pan, L. Xu, J. Zheng, Z. Gao, T. Hu, C. Meng, Electrochim. Acta 332 (2020) 135506–135516.
[140] Y.-K.S. Jae Hyeon Jo, Seung-Taek Myung, J. Mater. Chem. A 5 (2017) 8367–8375.
[141] Q.F. Li, D. Chen, Y.Z. Feng, N. Xiao, L.Y. Gan, Q. Zhang, Y. Yu, S.M. Huang, Nano-Micro Lett. 12 (2020) 67–78.
[142] X. Wang, B.J. Xi, X.J. Ma, Z.Y. Feng, Y.X. Jia, J.K. Feng, Y.T. Qian, S.L. Xiong, Nano Lett. 20 (2020) 2899–2906.
[143] C. Wang, S. Wei, S. Chen, D. Cao, L. Song, Small Methods 3 (2019) 1900495–1900503.
[144] H.Y. Wang, T.L. Hou, D. Sun, X.B. Huang, H.N. He, Y.G. Tang, Y.N. Liu, J. Power Sources 247 (2014) 497–502.
[145] Y.G. Tang, H. Qiao, H.Y. Wang, P.P. Tao, J. Mater. Chem. A 1 (2013) 12512–12518.
[146] D. Selvakumaran, A. Pan, S. Liang, G. Cao, J. Mater. Chem. A 7 (2019) 18209–18236.
[147] W. Liu, P. Liu, R. Hao, Y. Huang, X. Chen, R. Cai, J. Yan, K. Liu, ChemElectroChem 7 (2020) 1166–1171.
[148] J. Shi, S. Wang, Q. Wang, X. Chen, X. Du, M. Wang, Y. Zhao, C. Dong, L. Ruan, W. Zeng, J. Power Sources 446 (2020) 227345–227353.
[149] B. Liu, Y. Sun, L. Liu, S. Xu, X. Yan, Adv. Funct. Mater. 28 (2018) 1704973–1705006.
[150] C. Guo, H.M. Liu, S. Tian, B.L. Chen, J. Zhao, J.F. Li, Electrochim. Acta 324 (2019) 134867–134875.
[151] M.H. Alfaruqi, V. Mathew, J. Gim, S. Kim, J. Song, J.P. Baboo, S.H. Choi, J. Kim, Chem. Mater. 27 (2015) 3609–3620.
[152] D.H. Wang, L.F. Wang, G.J. Liang, H.F. Li, Z.X. Liu, Z.J. Tang, J.B. Liang, C.Y. Zhi, ACS Nano 13 (2019) 10643–10652.
[153] L.L. Wang, L.H. Xu, J.T. Chen, J.R. Zheng, ACS Sustain. Chem. & Eng. 6 (2018) 16055–16063.
[154] Y. Pan, M. Xu, L. Yang, M. Yu, H. Liu, F. Zeng, J. Alloys Compd. 819 (2020) 152969–152978.
[155] W. Jiang, X. Xu, Y. Liu, L. Tan, F. Zhou, Z. Xu, R. Hu, J. Alloys Compd. 827 (2020) 154273–154282.
[156] D.-S. Li, Q.-L. Gao, H. Zhang, Y.-F. Wang, W.-L. Liu, M.-M. Ren, F.-G. Kong, S.-J. Wang, J. Chang, Appl. Surf. Sci. 510 (2020) 145458–145467.
[157] B. He, Q. Zhang, L. Li, J. Sun, P. Man, Z. Zhou, Q. Li, J. Guo, L. Xie, C. Li, X. Wang, J. Zhao, T. Zhang, Y. Yao, J. Mater. Chem. A 6 (2018) 14594–14601.
[158] Y. Liu, X. Chi, Q. Han, Y. Du, J. Huang, Y. Liu, J. Yang, J. Power Sources 443 (2019) 227244–227251.
[159] B. Wu, G. Zhang, M. Yan, T. Xiong, P. He, L. He, X. Xu, L. Mai, Small 14 (2018) 1703850–1703857.
[160] C. Wang, X. Xiao, S.J. Wu, G.B. Zhong, K.Q. Xu, Z.F. Wei, W. Su, X.H. Lu, J. Energy Chem. 43 (2020) 182–187.
[161] J. Wang, J.-G. Wang, H. Liu, C. Wei, F. Kang, J. Mater. Chem. A 7 (2019) 13727–13735.
[162] M.S. Zhang, W.X. Wu, J.W. Luo, H.Z. Zhang, J. Liu, X.Q. Liu, Y.Y. Yang, X.H. Lu, J. Mater. Chem. A 8 (2020) 11642–11648.
[163] H. Peng, H. Fan, C. Yang, Y. Tian, C. Wang, J. Sui, RSC Adv. 10 (2020) 17702–17712.
[164] G.X. Liu, H.W. Huang, R. Bi, X. Xiao, T.Y. Ma, L. Zhang, J. Mater. Chem. A 7 (2019) 20806–20812.
[165] S. Yuan, W. Chen, L. Zhang, Z. Liu, J. Liu, T. Liu, G. Li, Q. Wang, Small 15 (2019) 1903311–1903319.
[166] B. Jiang, C. Xu, C. Wu, L. Dong, J. Li, F. Kang, Electrochim. Acta 229 (2017) 422–428.
[167] Y. Zhu, Y. Huang, M. Wang, C. Chen, Ceram. Int. 45 (2019) 24500–24507.
[168] P. Liu, K. Zhu, K. Bian, Y. Xu, F. Zhang, W. Zhang, J. Zhang, W. Huang, J. Alloys Compd. 765 (2018) 901–906.
[169] D. Feng, T.-N. Gao, L. Zhang, B. Guo, S. Song, Z.-A. Qiao, S. Dai, Nano-Micro Lett. 12 (2019) 14–26.
[170] L. Gou, K.L. Mou, X.Y. Fan, M.J. Zhao, Y. Wang, D. Xue, D.L. Li, Dalton Trans. 49 (2020) 711–718.
[171] A. Dhiman, D.G. Ivey, Batteries & Supercaps 3 (2019) 293–305.
[172] J. Hao, J. Mou, J. Zhang, L. Dong, W. Liu, C. Xu, F. Kang, Electrochim. Acta 259 (2018) 170–178.
[173] C. Zhu, G. Fang, J. Zhou, J. Guo, Z. Wang, C. Wang, J. Li, Y. Tang, S. Liang, J. Mater. Chem. A 6 (2018) 9677–9683.
[174] L. Li, J. Yang, H. Yang, L. Zhang, J. Shao, W. Huang, B. Liu, X. Dong, ACS Appl. Energy Mater. 1 (2018) 963–969.
[175] Y. Li, Y. Song, H. Wang, W. Yu, J. Wang, X. Dong, G. Liu, Q. Ma, New J. Chem. 44 (2020) 3888–3895.
[176] Y. Wang, S. Rao, P. Mao, F. Zhang, P. Xiao, L. Peng, Q. Zhu, Electrochim. Acta 337 (2020) 135739.
[177] H. Chen, W. Zhou, D. Zhu, Z. Liu, Z. Feng, J. Li, Y. Chen, J. Alloys Compd. 813 (2020) (1817) 151812–151815.
[178] Q.L. Gao, X.M. Liu, Y.F. Wang, W.L. Liu, M.M. Ren, F.G. Kong, S.J. Wang, R.C. Zhou, Electrochim. Acta 335 (2020) 135642–135652.
[179] M. Sun, D.S. Li, Y.F. Wang, W.L. Liu, M.M. Ren, F.G. Kong, S.J. Wang, Y.Z. Guo, Y. M. Liu, ChemElectroChem 6 (2019) 2510–2516.
[180] G. Yuan, M. Geng, P. Zhang, B. Li, J. Solid State Electrochem. 24 (2020) 601–607.
[181] X. Wu, Y. Li, C. Li, Z. He, Y. Xiang, L. Xiong, D. Chen, Y. Yu, K. Sun, Z. He, P. Chen, J. Power Sources 300 (2015) 453–459.
[182] S.T. James, C. Knight, A. Manthiram, J. Mater. Chem. A 3 (2015) 21077–21082.
[183] N. Zhang, F. Cheng, Y. Liu, Q. Zhao, K. Lei, C. Chen, X. Liu, J. Chen, J. Am. Chem. Soc. 138 (2016) 12894–12901.
[184] V. Soundharrajan, B. Sambandam, S. Kim, V. Mathew, J. Jo, S. Kim, J. Lee, S. Islam, K. Kim, Y.-K. Sun, J. Kim, ACS Energy Lett. 3 (2018) 1998–2004.
[185] L. Chen, Z. Yang, F. Cui, J. Meng, H. Chen, X. Zeng, Appl. Surf. Sci. 507 (2020) 145137–145143.
[186] Y. Liu, Z. Pan, D. Tian, T. Hu, H. Jiang, J. Yang, J. Sun, J. Zheng, C. Meng, Y. Zhang, Chem. Eng. J. 399 (2020) 125842–125850.
[187] W. Zhang, C. Tang, B. Lan, L. Chen, W. Tang, C. Zuo, S. Dong, Q. An, P. Luo, J. Alloys Compd. 819 (2020) 152971–152978.
[188] W. Zhou, M. Chen, A. Wang, A. Huang, J. Chen, X. Xu, C.-P. Wong, J. Energy Chem. 52 (2021) 377–384.
[189] C. Liu, W. Xu, C. Mei, M.-C. Li, X. Xu, Q. Wu, Chem. Eng. J. 405 (2021) 126737–126745.
[190] M. Tamilselvan, T.V.M. Sreekanth, K. Yoo, J. Kim, Appl. Surf. Sci. 529 (2020) 147077–147084.
[191] F. Tang, J. Gao, Q. Ruan, X. Wu, X. Wu, T. Zhang, Z. Liu, Y. Xiang, Z. He, X. Wu, Electrochim. Acta 353 (2020) 136570–136578.
[192] C. Zhu, G. Fang, S. Liang, Z. Chen, Z. Wang, J. Ma, H. Wang, B. Tang, X. Zheng, J. Zhou, Energy Storage Mater. 24 (2020) 394–401.
[193] C. Guo, S. Tian, B. Chen, H. Liu, J. Li, Mater. Lett. 262 (2020) 127180–127184.
[194] A. Huang, W. Zhou, A. Wang, M. Chen, Q. Tian, J. Chen, J. Energy Chem. 54 (2021) 475–481.